Polarimetric Signatures in Landfalling Tropical Cyclones

CAMERON R. HOMEYER,[a] ALEXANDRE O. FIERRO,[b,c] BENJAMIN A. SCHENKEL,[b,c] ANTHONY C. DIDLAKE JR.,[d] GREG M. MCFARQUHAR,[b,a] JIAXI HU,[b,c] ALEXANDER V. RYZHKOV,[b,c] JEFFREY B. BASARA,[a,e] AMANDA M. MURPHY,[a,b] AND JONATHAN ZAWISLAK[f,g]

[a] *School of Meteorology, University of Oklahoma, Norman, Oklahoma*
[b] *Cooperative Institute for Mesoscale Meteorological Studies, University of Oklahoma, Norman, Oklahoma*
[c] *NOAA/OAR/National Severe Storms Laboratory, Norman, Oklahoma*
[d] *Department of Meteorology and Atmospheric Science, The Pennsylvania State University, University Park, Pennsylvania*
[e] *School of Civil Engineering and Environmental Science, University of Oklahoma, Norman, Oklahoma*
[f] *Cooperative Institute for Marine and Atmospheric Studies, University of Miami, Miami, Florida*
[g] *NOAA/Atlantic Oceanographic and Meteorological Laboratory/Hurricane Research Division, Miami, Florida*

(Manuscript received 8 April 2020, in final form 26 October 2020)

ABSTRACT: Polarimetric radar observations from the NEXRAD WSR-88D operational radar network in the contiguous United States, routinely available since 2013, are used to reveal three prominent microphysical signatures in landfalling tropical cyclones: 1) hydrometeor size sorting within the eyewall convection, 2) vertical displacement of the melting layer within the inner core, and 3) dendritic growth layers within stratiform regions of the inner core. Size sorting signatures within eyewall convection are observed with greater frequency and prominence in more intense hurricanes, and are observed predominantly within the deep-layer environmental wind shear vector-relative quadrants that harbor the greatest frequency of deep convection (i.e., downshear and left-of-shear). Melting-layer displacements are shown that exceed 1 km in altitude compared to melting-layer altitudes in outer rainbands and are complemented by analyses of archived dropsonde data. Dendritic growth and attendant snow aggregation signatures in the inner core are found to occur more often when echo-top altitudes are low (≤10 km MSL), nearer the −15°C isotherm commonly associated with dendritic growth. These signatures, uniquely observed by polarimetric radar, provide greater insight into the physical structure and thermodynamic characteristics of tropical cyclones, which are important for improving rainfall estimation and the representation of tropical cyclones in numerical models.

KEYWORDS: Tropical cyclones; Cloud microphysics; Radars/Radar observations

1. Introduction

Tropical cyclones (TCs) are a considerable threat to coastal communities and the shipping industry each year. TCs undergoing changes in intensity and precipitation structure as they approach landfall pose an ongoing major challenge for operational forecasters (Gall et al. 2013; Rozoff et al. 2015). Because TC tracks are chiefly governed by the larger-scale, synoptic-scale environment (steering flow), recent advances in numerical weather prediction models and data assimilation techniques have largely accounted for a notable improvement in their forecast in the last few decades (Hendricks et al. 2011). Intensity predictions, however, have improved at half the rate as track forecasts over the same period (DeMaria et al. 2014) because intensity fluctuations are significantly influenced by forcing external to synoptic-scale environmental conditions (Molinari and Vollaro 1989; Bosart et al. 2000; Hanley et al. 2001) and, most importantly, by small-scale, transient, hard-to-forecast, moist convective processes in the TC inner core or eyewall. Many observational and modeling studies have indeed stressed the pivotal role of frequent, deep convective bursts in the TC inner core (e.g., Hendricks et al. 2004; Montgomery et al. 2006; Guimond et al. 2010; McFarquhar et al. 2012; Chen and Zhang 2013; Rogers et al. 2016; Hazelton et al. 2017) and eyewall replacement cycles (Sitkowski et al. 2011; Kossin and DeMaria 2016; Fischer et al. 2020) to TC intensification.

The intensification of TCs is closely related to the distribution and organization of convection around the TC center. It has long been known that strong deep-layer vertical wind shear is detrimental to the formation, intensification, and maintenance of TCs by disrupting convective axisymmetry in the inner core (e.g., Gray 1968; DeMaria 1996; Black et al. 2002). Observational works have shown that the azimuthal distribution of convection is highly dependent on the direction and strength of the deep-layer (850–200 hPa) environmental vertical wind shear (Corbosiero and Molinari 2002, 2003; Chen et al. 2006), with the most intense convection (and lightning) generally occurring within the downshear-left quadrant of the inner core under moderate-to-strong shear regimes (Chen et al. 2006; DeHart et al. 2014; Fierro and Mansell 2017). However, when the vertical tilt of the vortex is not aligned with the shear vector direction, deep convection can preferentially occur in other quadrants (e.g., upshear left, Stevenson et al. 2014). The response of the primary circulation to the shear controls the azimuthal distribution of convection, such that downshear tilt of the vortex (eyewall slope; Stern and Nolan 2009; Hazelton et al. 2015) can counteract this

Supplemental information related to this paper is available at the Journals Online website: https://doi.org/10.1175/MWR-D-20-0111.s1.

Corresponding author: Cameron R. Homeyer, chomeyer@ou.edu

DOI: 10.1175/MWR-D-20-0111.1

© 2021 American Meteorological Society. For information regarding reuse of this content and general copyright information, consult the AMS Copyright Policy (www.ametsoc.org/PUBSReuseLicenses).

Brought to you by NOAA Central Library | Unauthenticated | Downloaded 01/14/21 02:34 PM UTC

vertical misalignment through an enhanced secondary circulation downshear (Jones 1995; Frank and Ritchie 1999; Reasor et al. 2004). Several mechanisms have been put forth to account for the resiliency of the primary vortex to tilt, which includes upshear precession of the vortex (Jones 1995) and vortex Rossby wave damping (e.g., Reasor and Montgomery 2001; Schecter et al. 2002).

Broadly, shear is associated with inner-core (azimuthal) asymmetries (generally of wavenumber 1, Reasor et al. 2000) in vertical velocity, surface convergence, and accumulated rainfall (Frank and Ritchie 1999; Black et al. 2002; Rogers et al. 2003). More specifically, convection, maximum sustained winds at the surface, and rainfall in the inner core of a TC generally organizes to the left of the shear vector relative to the downshear direction (Willoughby et al. 1984; Marks et al. 1992; Franklin et al. 1993; Gamache et al. 1997; Corbosiero and Molinari 2002; Black et al. 2002; Eastin et al. 2005; Reasor et al. 2009, 2013; Uhlhorn et al. 2014; Fierro and Mansell 2017). Updrafts initiated downshear right, where low- to midtropospheric convergence is favored by the shear, ultimately result in a maximum vertical motion in the downshear-left quadrant upon cyclonic revolution around the core by the (primary) tangential circulation (e.g., Braun and Wu 2007; Hence and Houze 2012; DeHart et al. 2014).

The relationship between convective processes (ultimately latent heating), TC intensification, and TC precipitation is largely influenced by the evolution of the TC microphysics. It is well known that, at a given grid spacing, TC intensity and precipitation structure in model simulations is particularly sensitive to the chosen microphysics parameters and scheme within the simulation (e.g., Lord et al. 1984; McFarquhar et al. 2006; Fierro et al. 2009; Brown et al. 2016; Fierro and Mansell 2017; Wang et al. 2020). It is critical that such parameterizations are constrained by accurate and thorough observations of TC microphysics. Past observational studies have shown that the inner core of TCs is generally dominated by warm rain processes (Jorgensen et al. 1985) characterized by a sharp decrease in radar reflectivity with height (Cecil et al. 2002). Jorgensen et al. (1985) argued that early fallout of the majority of the liquid water from the updraft before the particles freeze is consistent with a generally weak updraft ($<5\,m\,s^{-1}$, Zipser and Lutz 1994) near the freezing level. Black (1984) showed that little liquid water was found within the updrafts significantly above the freezing level in hurricanes Allen (1980) and Irene (1981), which reduces the potential for significant rimed ice formation such as graupel or hail. In fact, most of the supercooled liquid water that subsists above the freezing level becomes frozen before the temperature reaches −10°C, indicating a rapid glaciation of the cloud (Black and Hallett 1986).

Willis and Heymsfield (1989) hypothesized that in the inner core of the TC, the graupel that is largely confined to convective regions is actively involved in secondary nucleation (i.e., the Hallett–Mossop mechanism; Hallett and Mossop 1974), providing an abundant supply of ice crystals for aggregation outside the convective region (Marks and Houze 1987; Houze et al. 1992). This is consistent with the study of Black and Hallett (1986) who found that most of the ice within eyewall updrafts originates from the ''ice multiplication'' mechanism. These small ice particles are then redistributed throughout the storm by the upper- and midtropospheric circulations.

An improved understanding and model representation of TC microphysics is likely to improve our ability to predict related hazards during landfall including extreme precipitation such as that observed with recent hurricanes Harvey (2017; Wolff et al. 2019; Brauer et al. 2020) and Florence (2018). The operational weather radar network in the United States—Next Generation Weather Radar (NEXRAD)—was created in 1957 to monitor clouds and precipitation. Beginning in 1988, the network was upgraded to Doppler S-band (10–11.1 cm wavelength) horizontal polarization radars—named Weather Surveillance Radar-1988 Doppler (WSR-88D; Crum and Alberty 1993). The WSR-88D network, which includes 143 radars in the contiguous United States (CONUS), was again upgraded between 2011 and 2013 to transmit in horizontal *and* vertical polarization (dual-polarization or polarimetric). The new polarimetric variables observed by the upgraded NEXRAD WSR-88D network enable considerable improvements in the discrimination between meteorological and nonmeteorological scatterers as well as between various precipitation types (e.g., rain, snow, hail) by providing information on the size, shape, phase, and concentration of scatterers. Given the recent upgrade of the NEXRAD network to dual-polarization and the occurrence of several high-impact landfalling TCs since that time, there exists a unique opportunity to more systematically analyze microphysical observations of TCs to better understand in-cloud hydrometeor structure, variability, and utility in assessing rainfall rates and potential hazards.

Given the emerging stage of this research, recent work aimed at leveraging the unique potential of polarimetric radar observations to understand TC microphysics has been primarily focused on individual case studies. For example, Van Den Broeke (2013) identified unique signatures of biological scatterers in the eyes of Hurricanes Irene (2011) and Sandy (2012) using polarimetric observations from the NEXRAD network, indicating a likely association with oceanic birds based on inland ground reports. Griffin et al. (2014) used polarimetric observations from the prototype WSR-88D in Norman, OK to diagnose the microphysical and electrical characteristics of the remnants of Tropical Storm Erin (2007) and its reintensification over Oklahoma, arguing from these perspectives that inner-core convection was critical to the reintensification. Didlake and Kumjian (2017, 2018) leveraged polarimetric observations from NEXRAD to examine the bulk microphysics in relation to storm kinematics and asymmetries for Hurricanes Arthur (2014) and Irma (2017), respectively, and found unique polarimetric indications of transitions between convection and stratiform precipitation and size sorting within primary and secondary eyewall regions. Feng and Bell (2019) also analyzed the size sorting in the eyewall of Hurricane Harvey (2017) and estimated the associated drop size distribution (DSD) in different areas of the eyewall.

Several recent studies have placed emphasis on more detailed and extensive microphysics retrievals, including drop diameter and concentration, for inner and outer rainbands in

Brought to you by NOAA Central Library | Unauthenticated | Downloaded 01/14/21 02:34 PM UTC

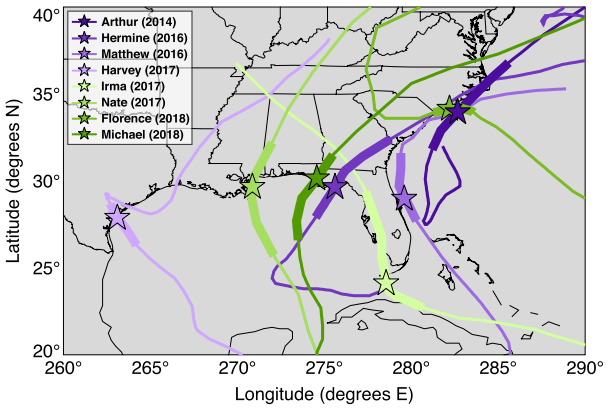

FIG. 1. Map of storm tracks. Stars indicate the locations of each storm at the time of analysis in Figs. 2–4. The thicker segments overlaid on the tracks indicate each TC's center location used for analysis in this study.

TCs using polarimetric radar and disdrometer observations. Wang et al. (2016, 2018) and Wen et al. (2018) utilized polarimetric radar observations in several landfalling typhoons in China to demonstrate the dominance of warm rain processes and small- to medium-sized (1–2 mm diameter) drops within outer rainbands, in agreement with many previous studies using alternative data. Wang et al. (2018) further revealed that within outer rainbands there is a transition between precipitation dominated by warm rain processes in convective updraft regions to precipitation dominated by melting of convectively generated graupel outside of the updrafts, while Wu et al. (2018) revealed that there is an increase in the importance of riming (i.e., graupel production) to heavy rainfall in outer rainbands compared to that in inner stratiform bands. Hu et al. (2020) revealed the same tendency of increased graupel production in the outer rainbands of Hurricanes Harvey (2017) and Florence (2018) in the United States, while DeHart and Bell (2020) carried out microphysics retrievals for these TCs and revealed once again that precipitation is broadly dominated by warm rain processes but indicated that raindrop concentrations are about an order of magnitude smaller than those found in the landfalling typhoons in China.

To continue to improve understanding of the microphysical characteristics of TCs using polarimetric radar observations, a broader investigation into commonalities and differences between storms with various intensities and environmental conditions is required. In this study, we examine polarimetric radar observations from the NEXRAD WSR-88D network during eight recent landfalling hurricanes in the CONUS: Arthur (2014), Hermine (2016), Matthew (2016), Harvey (2017), Irma (2017), Nate (2017), Florence (2018), and Michael (2018). A map of storm tracks from these eight TCs is shown in Fig. 1. By leveraging lower-tropospheric maps, vertical profiles, and unique data processing techniques, we identify coherent and consistent signatures in the polarimetric radar variables that reveal new information on the physical and thermodynamic characteristics of TCs at and near landfall. The results presented in the following sections have important implications for future research and numerical modeling of TCs, especially for storm-scale and mesoscale impacts on coastal and inland areas near the landfalling location.

2. Data and methods

a. Radar observations

As outlined in section 1, the relatively recent upgrade of the NEXRAD WSR-88D network to dual-polarization provides a unique opportunity to analyze in detail scatterers contained within radar sample volumes. Each polarimetric radar within the NEXRAD network samples precipitation at approximately 5-min intervals on a polar grid with a range resolution of 250 m, an azimuthal resolution of 0.5° in the lowest three to five elevations and 1.0° aloft, with measurements obtained at 14 elevations in most cases (especially when the precipitation column is deep). The variables measured by the polarimetric WSR-88Ds include radar reflectivity factor at horizontal polarization (Z_H), radial Doppler velocity (V_R), velocity spectrum width (σ_V), the differential radar reflectivity factor (Z_{DR}), differential phase (ϕ_{DP}), and the copolar correlation coefficient (ρ_{HV}). This study focuses on analysis of four microphysical variables (Z_H, Z_{DR}, ϕ_{DP}, and ρ_{HV}). Note that rather than performing a direct analysis of ϕ_{DP}, we compute half the range derivative of ϕ_{DP}, a key polarimetric variable commonly known as the specific differential phase, or K_{DP} (Seliga and Bringi 1978).

The polarimetric variables used in this study provide information on the characteristics of anisotropic particles that can be used to elucidate important microphysical and/or dynamical processes taking place within cloudy areas of TCs. Specifically, Z_H is dependent on hydrometeor concentration and size given its proportionality to the sixth moment of the observed particle size distribution for rain and approximately the fourth moment for snow; Z_{DR}—the logarithmic difference between reflectivity factors at horizontal and vertical polarizations—provides a reflectivity-weighted indication of average particle shape, orientation, and/or phase composition; K_{DP} relates to the total mass of nonspherical particles; and ρ_{HV} indicates the diversity of particle type and phase within the sample volume. Moreover, combinations of the polarimetric variables can help to reveal the significance and occurrence of unique microphysical processes at work within storms and retrieve common microphysical parameters (see end of this subsection), especially when thermodynamic properties of the environment are known. Additional detailed descriptions of the polarimetric variables and their physical meaning can be found in several textbooks (e.g., Doviak and Zrnić 1993; Bringi and Chandrasekar 2001; Ryzhkov and Zrnić 2019) and review papers (e.g., Herzegh and Jameson 1992; Hubbert et al. 1998; Zrnić and Ryzhkov 1999; Straka et al. 2000; Ryzhkov et al. 2005b; Kumjian 2013a,b,c).

All NEXRAD WSR-88D data analyzed in this study were obtained from the National Centers for Environmental Information (NOAA/NWS/ROC 1991). Analysis of NEXRAD data in the remainder of this work is performed using three analysis techniques: (i) merged polarimetric volumes from multiple radars via the Gridded NEXRAD WSR-88D Radar (GridRad; http://gridrad.org) space- and time-weighted binning

Brought to you by NOAA Central Library | Unauthenticated | Downloaded 01/14/21 02:34 PM UTC

algorithm (Homeyer and Bowman 2017), (ii) quasi-vertical profiles (QVPs) from azimuthally averaged high-elevation radar scans (e.g., Ryzhkov et al. 2016), and (iii) columnar vertical profiles (CVPs) from range and azimuth restricted sectors of full volume scans (Murphy et al. 2020). While an hourly archive of Z_H-only GridRad data are publicly available (Bowman and Homeyer 2017), a unique set of polarimetric GridRad data are created at 5-min intervals on a $\sim 0.02° \times 0.02°$ longitude–latitude grid, with 0.5 km vertical grid spacing from 1 to 7 km and 1 km vertical grid spacing above that for all analyzed TCs. Similar polarimetric GridRad data have been created and analyzed for microphysical studies in Homeyer and Kumjian (2015) and Handler and Homeyer (2018). These data provide large-area depictions of cloud microphysics that are not possible via analysis of observations from a single radar. We use GridRad data to investigate the scale and robustness of identified polarimetric signatures and characteristics, primarily through long-duration composite analyses. To identify convection and stratiform precipitation within each TC, we apply the Storm Labeling in Three Dimensions (SL3D) algorithm (Starzec et al. 2017) to the GridRad data, which was developed using GridRad data and demonstrated good reliability in both midlatitude storms and TCs over the CONUS.

To merge and analyze the polarimetric variables in GridRad data, several important quality-control techniques are applied. First, only observations with $\rho_{\mathrm{HV}} > 0.5$ are merged into GridRad volumes to limit deleterious impacts from contributions of nonmeteorological scatterers. Second, K_{DP} is calculated using first-order centered differencing of ϕ_{DP} observations that are first smoothed using a 7.5-km radial running-mean filter to reduce random noise. Third, Z_{DR} observations from each radar are objectively bias-corrected prior to binning by using observations of snow aggregates and a "natural scatterer" approach (e.g., Ryzhkov et al. 2005a). An exhaustive review of these techniques and reasoning for their application is provided in Homeyer and Kumjian (2015). Following creation, all GridRad data undergo two quality-control steps before analysis. First, echoes are removed if they occur within a GridRad volume sampled infrequently by NEXRAD WSR-88D radars and/or only at large distances from contributing radar locations (this process is described in further technical detail within Homeyer and Bowman (2017) and is referred to as "filtering"). Second, echoes are discarded if $Z_H < 40\,\mathrm{dBZ}$ and $\rho_{\mathrm{HV}} < 0.9$, which eliminates the vast majority of nonmeteorological scatterers that remain.

In this study, time–height analyses are created using QVPs, profiles from select locations within GridRad data volumes (in the supplemental material), and CVPs. QVPs provide azimuthally averaged observations of high elevation scans (those $>10°$) from a single radar, resulting in instantaneous high-resolution "profiles" of radar variables that reduce inhomogeneities and/or noise in the physical variables that are inherent to short-duration pulses of operational radars (e.g., Kumjian et al. 2013; Trömel et al. 2013, 2014; Ryzhkov et al. 2016; Tobin and Kumjian 2017). When computing QVPs from a continuous set of radar volumes, these provide detailed time–height depictions (i.e., curtains) of the radar variables that enable understanding of the dominant microphysical processes occurring throughout the vertical dimension of a storm. QVPs are ideal for studying broad regions of precipitation that are horizontally homogeneous (i.e., stratiform precipitation) and have become increasingly used for research. For example, recent efforts have leveraged QVPs to study microphysical processes and signatures such as those in and near the melting layer of stratiform precipitation within mesoscale convective systems (e.g., Kumjian et al. 2016) and precipitation types and growth processes within winter storms (e.g., Van Den Broeke et al. 2016; Kumjian and Lombardo 2017; Griffin et al. 2018). Here, we leverage the QVP method to analyze the broad physical characteristics of TCs from two storms that passed within close proximity to a NEXRAD WSR-88D site during landfall.

Time–height analyses using the CVP method are also calculated and designed to coincide with the track of TCs as they pass by. Since CVPs are based on a single point (column) within a radar's domain, they provide a less vertically resolved depiction of storm microphysics and their variability with altitude compared to that from QVPs. Despite this limitation, bulk microphysical characteristics are diagnosed reasonably well, as summarized in the remainder of this work. The GridRad time–height analyses in the supplemental material are comparable to these CVPs.

The CVPs produced for this study were used for rain and ice microphysics retrieval. The retrieval, based on work outlined in Ryzhkov et al. (2018, 2020) and Ryzhkov and Zrnić (2019)—their chapter 11, summarized briefly below, provide estimates of liquid water content (LWC) in rain, ice water content (IWC) in ice, mean volume diameter D_m, and total number concentration N_t. Equations relating the polarimetric variables to the retrieved quantities are defined as follows:

In rain,

$$\mathrm{LWC} = 1.38 \times 10^{-3} \quad Z_h \times 10^{(-2.43 Z_{\mathrm{DR}} + 1.12 Z_{\mathrm{DR}}^2 - 0.17 Z_{\mathrm{DR}}^3)}, \tag{1}$$

$$D_m = 0.171 Z_{\mathrm{DR}}^3 - 0.725 Z_{\mathrm{DR}}^2 + 1.48 Z_{\mathrm{DR}} + 0.717, \tag{2}$$

$$\log_{10}(N_t) = -2.37 + 0.1 Z_h - 2.89 Z_{\mathrm{DR}} + 1.28 Z_{\mathrm{DR}}^2 - 0.213 Z_{\mathrm{DR}}^3; \tag{3}$$

in ice,

$$\mathrm{IWC} = 4 \times 10^{-3} \left(\frac{K_{\mathrm{DP}} \lambda}{1 - Z_{\mathrm{dr}}^{-1}} \right), \tag{4}$$

$$D_m = -0.1 + 2.0 \left(\frac{Z_{\mathrm{DP}}}{K_{\mathrm{DP}} \lambda} \right)^{1/2}, \tag{5}$$

$$\log_{10}(N_t) = 0.1 Z_H - 2 \log_{10} \left(\frac{Z_{\mathrm{DP}}}{K_{\mathrm{DP}} \lambda} \right) - 1.11, \tag{6}$$

where Z_h and Z_v are the horizontal and vertical radar reflectivity factors in linear units ($\mathrm{mm^6\,m^{-3}}$), respectively; Z_{dr} is the differential reflectivity in linear units, $Z_{\mathrm{DP}} = Z_h - Z_v$, and λ is the radar wavelength in mm. The retrieved LWC and IWC are in $\mathrm{g\,m^{-3}}$, D_m is in mm, and N_t is in $\mathrm{L^{-1}}$.

Equations (1)–(3) were derived using more than 47 000 DSDs obtained by a 2D-video disdrometer in central Oklahoma (Schuur et al. 2005) and are applicable to both convective and stratiform rain. Based on comparisons with these disdrometer

Brought to you by NOAA Central Library | Unauthenticated | Downloaded 01/14/21 02:34 PM UTC

observations, the LWC estimate from Eq. (1) has a fractional standard deviation (FSD) of ~35% for LWC varying from 0.1 to 1.0 g m^{-3}. The standard deviation of the D_m estimate from Eq. (2) increases with D_m, but the FSD is constant at ~10%. The standard deviation of the $\log_{10}(N_t)$ estimate from Eq. (3) is ~0.3 for the majority of DSDs and tends to be larger for very high [$\log_{10}(N_t) > 0$] and very low [$\log_{10}(N_t) < -1$] raindrop concentrations.

Equations (4)–(6) were obtained theoretically using scattering computations for 12 ice habits assuming a multitude of gamma size distributions, aspect ratios, orientations, and degrees of riming and are mainly applicable to stratiform precipitation without much graupel aloft. The derivations assume that the bulk density of ice or snow is inversely proportional to the particle's equivolume diameter, as in Brandes et al. (2007). The ratio Z_{DP}/K_{DP} in Eqs. (4)–(6) is very robust with respect to the variability of particle aspect ratios and orientations because these factors affect Z_{DP} and K_{DP} similarly, and, therefore, the ratio remains almost intact (Ryzhkov et al. 1998). Equations (4)–(6) are somewhat sensitive to the variability of the assumed degree of riming of snow and changes of the shape parameter μ of the gamma size distributions. Theoretical simulations show that the FSD of the IWC estimate from Eq. (4) is within 20% if $-1 < \mu < 1$, and IWC tends to be overestimated for $\mu < -1$, while the estimate is almost insensitive to the degree of riming. For a given degree of riming, the accuracy of the D_m estimate from Eq. (5) is within 20%. The accuracy of the $\log_{10}(N_t)$ estimate from Eq. (6) is dependent on the accuracy of the D_m retrieval and may vary from 0.7 to 1.0 (in log units) if D_m is estimated with an accuracy of 20%.

b. Tropical cyclone tracks

Longitudes, latitudes, and intensities at a minimum of 6-h intervals along the path of each storm analyzed here are obtained from the National Hurricane Center's second-generation North Atlantic hurricane database (HURDAT2; Landsea and Franklin 2013). For times in between available track information where storm locations are desired, we linearly interpolate storm positions in time from the HURDAT2 tracks.

c. Environmental assimilations

To compute the 850–200 hPa wind shear (direction and magnitude) necessary for all shear-relative quadrant analyses, this work employs 6-hourly assimilations from the European Centre for Medium-Range Weather Forecasts (ECMWF) interim reanalysis (ERA-Interim; Dee et al. 2011). ERA-Interim provides atmospheric state variables on a ~0.75° × 0.75°Gaussian longitude–latitude grid with 61 vertical levels. The vertical coordinate is a hybrid sigma–pressure coordinate that results in a vertical resolution ranging from approximately 250–1000 m throughout the troposphere. For analysis at intermediate times (e.g., hourly intervals), all ERA-Interim data are first interpolated linearly in space and time on the native model grid. To compute the 850–200 hPa wind shear vectors, profiles of zonal and meridional wind speeds are extracted within radial distances ranging from 200 to 800 km relative to storm center locations estimated from the HURDAT2 cyclone tracks. We use the azimuthal-mean shear vector from these profiles at hourly intervals along each storm track to partially circumvent the influence of the primary circulation from the TC. This approach is similar to that outlined in studies such as Kaplan and DeMaria (2003), Chen et al. (2006), and Hence and Houze (2011) using alternative forecast models or reanalysis model output.

d. Dropsonde data

Global positioning system (GPS) dropsonde data from the Tropical Cyclone–Dropsonde Research and Operations Product Suite (TC-DROPS; Nguyen et al. 2020) during 1996–2019 (N = 2697 sondes in 111 TCs) are used to quantify changes in altitudes of the 0° and −15°C isotherms with TC intensity, as a function of distance from storm center. We choose to use this larger dataset rather than the eight cases included in the radar analysis since sonde coverage can be limited for such a small group of storms and to provide a large enough sample to statistically examine changes in these two isotherms. TC-DROPS is a collection of sondes from: 1) operational NOAA and Air Force aircraft reconnaissance including those from the NOAA-DHA Long-term Dropsonde Hurricane archive (Wang et al. 2015) and 2) various NASA, ONR, NSF, and NOAA-sponsored field experiments including most recently the NOAA and NSF-sponsored Sensing Hazards with Operational Unmanned Technology (SHOUT; Dunion et al. 2018) and NASA-sponsored east Pacific Origins and Characteristics of Hurricanes (EPOCH; Emory et al. 2015) campaigns. Each dropsonde has been quality-controlled by the National Center for Atmospheric Research (NCAR) Earth Observing Laboratory (EOL) or the NOAA Atlantic Oceanographic and Meteorological Laboratory (AOML) Hurricane Research Division (HRD) using NCAR/EOL's Aspen sonde processing software, as well as additional manual quality-control steps. The radial distance from the TC center is determined for each dropsonde by interpolating the HURDAT2 cyclone track locations to the time of measurement.

3. Results

a. Summary of cases

As outlined in section 1, this study focuses on eight recent TCs that were densely observed by the polarimetric NEXRAD WSR-88D network as they approached and/or made landfall in the CONUS at hurricane strength on the Saffir–Simpson scale. While the storm tracks and key time periods used for the analysis of each case are identified in Fig. 1, a brief summary of the time periods analyzed in this study and corresponding characteristics of each storm is provided here.

Table 1 summarizes the following key characteristics of each storm: the time period(s) the TC was a hurricane, the first U.S. landfall time and location, maximum intensity reached (sustained wind speed and category on the Saffir–Simpson scale), the focal time of analysis (chosen to be near the time of first U.S. landfall and in most cases near the earliest times at which the TC is within range of multiple NEXRAD radars), and the maximum storm-relative range of the eyewall convection during the focal time of analysis. While many of the TCs analyzed were major hurricanes [sustained wind ≥96 kt (1 kt ≈ 0.51 m s^{-1}) and category ≥3] at one point during their life cycle, the times analyzed comprise four weak TCs (Hurricanes

Brought to you by NOAA Central Library | Unauthenticated | Downloaded 01/14/21 02:34 PM UTC

TABLE 1. For each TC analyzed: time periods when sustained winds exceeded the minimum threshold for a hurricane (≥64 kt), initial U.S. landfall time and location, the maximum intensity reached [sustained wind speed with the category (Cat) in parentheses on the Saffir–Simpson scale: 1, sustained wind 64–83 kt; 2, 84–95 kt; 3, 96–112 kt; 4, 113–136 kt; and 5, ≥137 kt), and the focal time of analysis in this study (and corresponding intensity]. All details except for the maximum range of eyewall convection were obtained from the HURDAT2 track dataset, with eyewall convection ranges determined subjectively from radar analysis at the focal time of analysis.

Hurricane	Period of hurricane strength	First U.S. landfall time (location)	Max intensity	Focal time of analysis (intensity)	Max range of eyewall
Arthur	3–5 Jul 2014	Near 0300 UTC 4 Jul (North Carolina)	85 kt (Cat 2)	~0000 UTC 4 Jul (85 kt; Cat 2)	50 km
Hermine	1–2 Sep 2016	Near 0530 UTC 2 Sep (Florida Panhandle)	70 kt (Cat 1)	0330 UTC 2 Sep (70 kt; Cat 1)	60 km
Matthew	29 Sep–9 Oct 2016	Near 1500 UTC 8 Oct (South Carolina)	145 kt (Cat 5)	1300 UTC 7 Oct (105 kt; Cat 3)	60 km
Harvey	24–26 Aug 2017	Near 0300 UTC 26 Aug (Texas)	115 kt (Cat 4)	0200 UTC 26 Aug (115 kt; Cat 4)	35 km
Irma	31 Aug–11 Sep 2017	Near 1300 UTC 10 Sep (Florida Keys)	155 kt (Cat 5)	0930 UTC 10 Sep (115 kt; Cat 4)	45 km
Nate	7–8 Oct 2017	Near 0000 UTC 8 Oct (Louisiana)	80 kt (Cat 1)	0230 UTC 8 Oct (75 kt; Cat 1)	60 km
Florence	4–6 and 9–14 Sep 2018	Near 1115 UTC 14 Sep (North Carolina)	130 kt (Cat 4)	1100 UTC 14 Sep (80 kt; Cat 1)	35 km
Michael	8–11 Oct 2018	Near 1730 UTC 10 Oct (Florida Panhandle)	140 kt (Cat 5)	1800 UTC 10 Oct (135 kt; Cat 4)	35 km

Arthur, Hermine, Nate, and Florence) and four strong TCs (i.e., major hurricanes; Hurricanes Matthew, Harvey, Irma, and Michael).

In each of the following subsections, we use polarimetric radar observations to outline several microphysical signatures that are repeatedly observed within the eight TCs of interest. Many unique signatures are present within the inner core of each storm and reveal microphysical and thermodynamic detail that, to the best of our knowledge, has not yet been extensively documented in prior work. Focus is first directed on signatures within the eyewall convection of each TC and then geared toward signatures within the broader domain of the inner core. These polarimetric signatures are then summarized in an idealized conceptual model for TCs.

b. *Lower-tropospheric maps*

Maps containing column-maxima of the polarimetric variables within the 1–4 km MSL layer (hereafter lower-tropospheric maps) reveal important signatures within the eyewall convection of each TC. To establish broader context, we first present a large-area lower-tropospheric map of Z_H from each TC in Fig. 2. This map demonstrates that each storm has unique structure, scale, and organization. Hurricane Hermine features the broadest and least organized eye and all TCs show significant asymmetry in the eyewall convection and/or the broader rain region. In each of these cases, a clear rainband complex is present within an ~150 km radius (i.e., within the superimposed black boxes), but Hurricane Irma appears to have a somewhat broader rainband complex than the remaining TCs. As in Willoughby et al. (1984), we define a storm's "inner core" as the region spanned by the innermost rainband complex (e.g., see Fig. 30 in Houze 2010). To reveal important polarimetric signatures within the eyewall convection of the inner core, Fig. 3 provides lower-tropospheric maps of Z_H, Z_{DR}, and K_{DP} within the black boxes of Fig. 2.

The inner-core lower-tropospheric maps (Fig. 3) reveal consistent polarimetric signatures within the eyewall convection of each storm. Namely, $Z_H > 40$ dBZ near storm center outlines well the prominent convective regions within each storm's eyewall (diagnosed by analysis of echo vertical extent, not shown). Embedded within and upstream of the eyewall Z_H maxima are regions of enhanced Z_{DR} (≥1 dB) and K_{DP} (≥0.33° km^{-1}), which are azimuthally offset from one another. Considering the strong primary cyclonic circulation of each TC at low levels, enhanced Z_{DR} zones are found both upstream of and overlapping enhanced K_{DP} areas. This azimuthal offset of Z_{DR} and extension of K_{DP} signatures is robust evidence of hydrometeor size sorting within the eyewall convection, as diagnosed further for Harvey in Feng and Bell (2019). The Z_{DR} enhancement, which extends slightly upstream of the 40 dBZ Z_H region in several of the more intense TCs analyzed (Hurricanes Matthew, Harvey, and Irma), is coincident with the expected location of convection initiation and maturation within the eyewall, where the strongest upward motion would be located and the largest drops formed (given the long established relationship between drop size and terminal velocity; Gunn and Kinser 1949). Due to the strong azimuthal circulation and the vertical nature of the secondary circulation, the smaller (and, hence, lower terminal velocity) drops formed in

Brought to you by NOAA Central Library | Unauthenticated | Downloaded 01/14/21 02:34 PM UTC

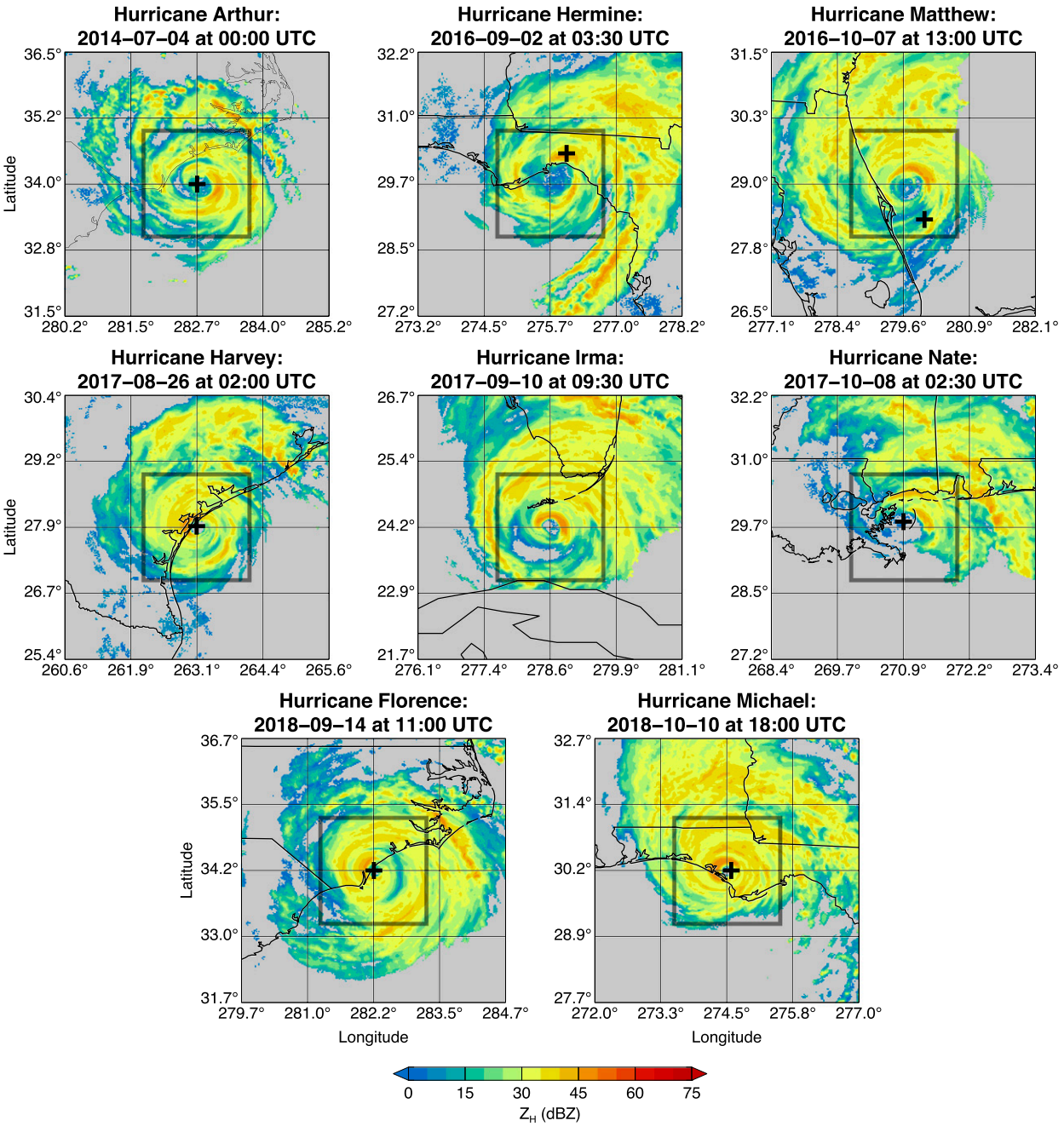

FIG. 2. Map of merged lower-tropospheric (column maxima in a layer 1–4 km MSL) Z_H from GridRad data. The thick black squares centered on each storm represent the extent of the domains used for Fig. 3. Thick black plus symbols indicate the locations of the GridRad time–height curtains included in the online supplemental material, with the only exception being Hurricane Irma (location is off the map at 27.5°N, 278.05°E).

the convective cells are transported longer distances through the cyclone and reach the surface at a location downstream of the largest drops, which is consistent with that implied by the azimuthal offset of the K_{DP} enhancement (representing high concentrations of smaller raindrops). Additional microphysical processes such as drop–drop collisions, growth (coalescence), and droplet breakup are anticipated to occur more readily at these altitudes in TCs, but such processes are more influential on variability in the radar variables in altitude rather than in the horizontal dimension.

The polarimetric signature of size sorting within the eyewall convection identified in these storms appears to reveal some noteworthy sensitivity to storm intensity and environmental wind shear. In particular, the size sorting signature is least

Brought to you by NOAA Central Library | Unauthenticated | Downloaded 01/14/21 02:34 PM UTC

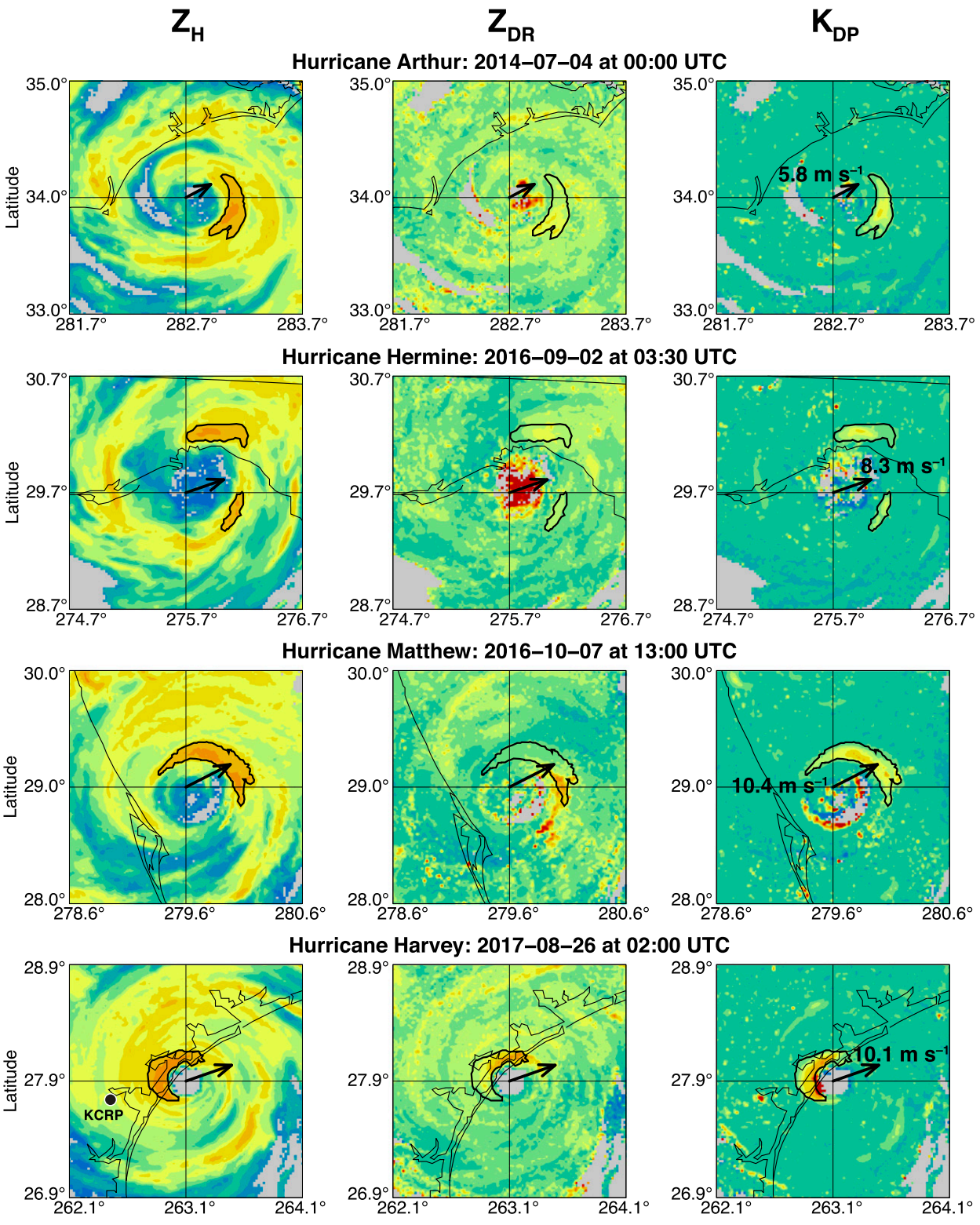

FIG. 3. Lower-tropospheric maps (column maxima in a layer 1–4 km MSL) of three polarimetric variables—(from left to right) Z_H, Z_{DR}, and K_{DP}—from GridRad data (from top to bottom) for each TC analyzed in this study (in chronological order). Thick black arrows superimposed on each map represent the direction and magnitude (length) of the 850–200 hPa wind shear vector, with the precise magnitudes of the shear vectors labeled in the K_{DP} maps. Thick black contours in each map outline the 40 dBZ Z_H contour corresponding to eyewall convection. Radars used for QVP analysis in Fig. 5 are shown by the large black labeled circles in the Z_H maps for Hurricanes Harvey and Irma.

Brought to you by NOAA Central Library | Unauthenticated | Downloaded 01/14/21 02:34 PM UTC

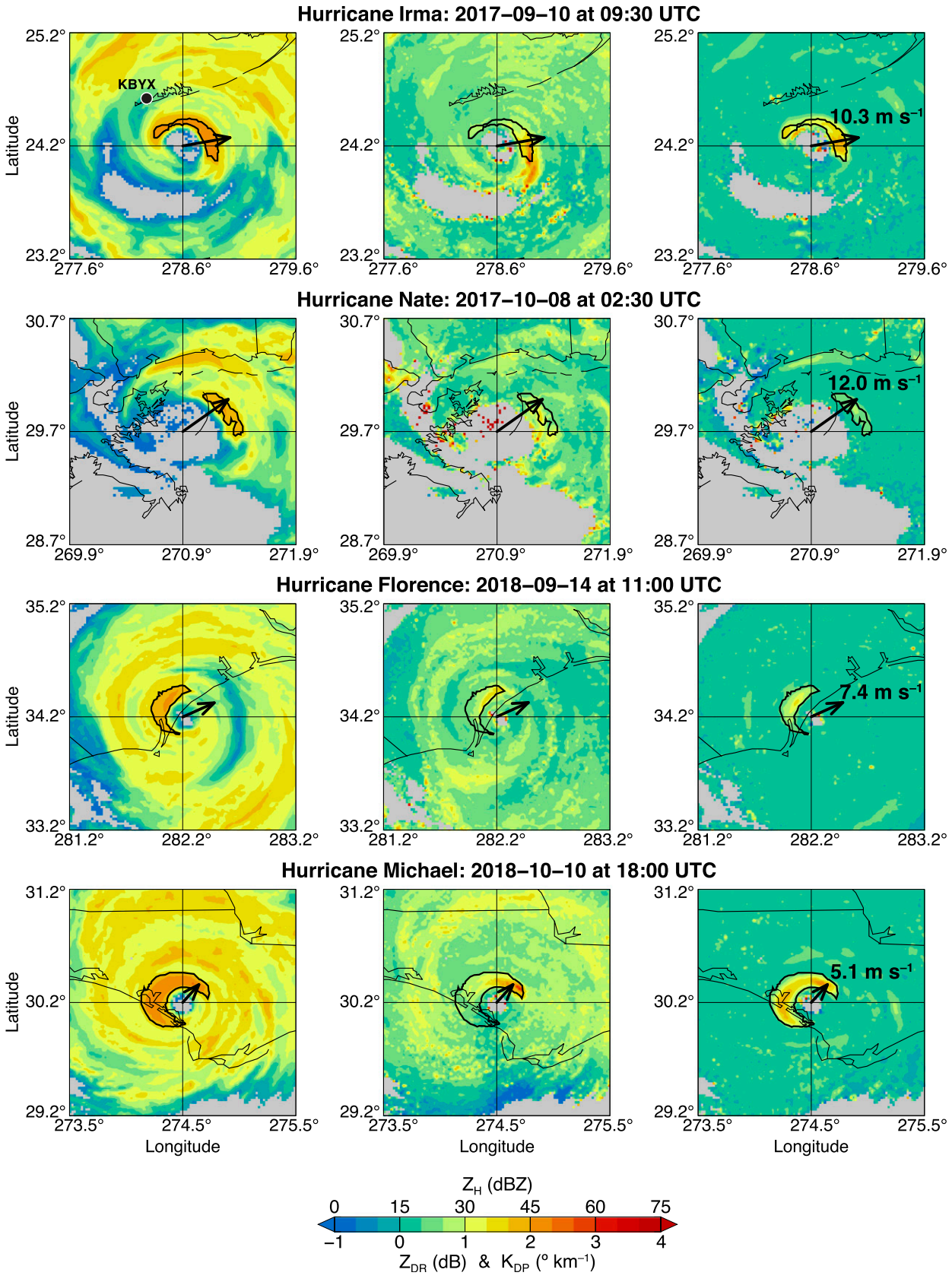

FIG. 3. (*Continued*)

Brought to you by NOAA Central Library | Unauthenticated | Downloaded 01/14/21 02:34 PM UTC

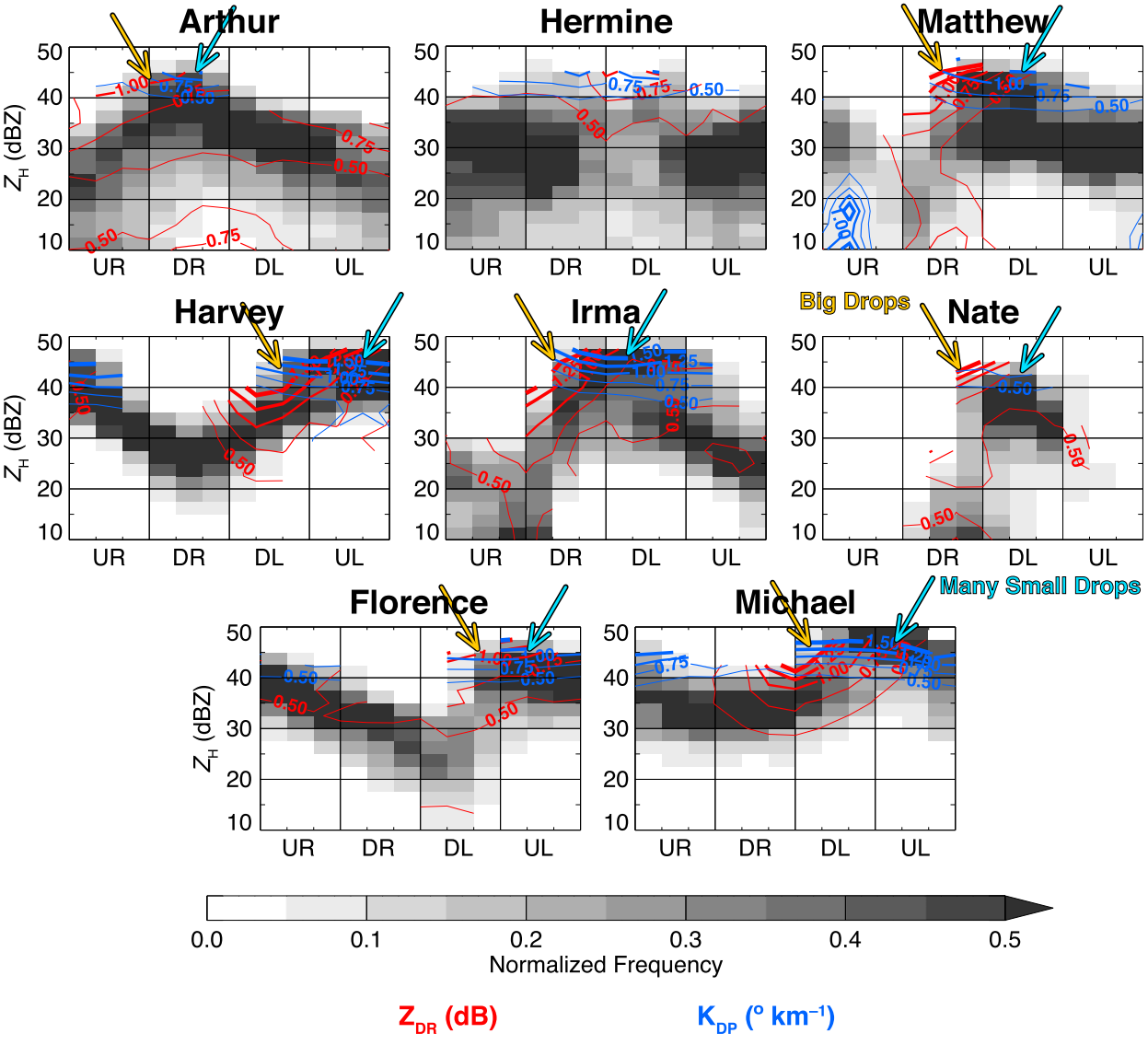

FIG. 4. Two-dimensional density diagrams (or histograms) of lower-tropospheric (1–4 km MSL) Z_H as a function of azimuth relative to storm center and the deep-layer shear vector, with shear-relative quadrants (from left to right in each panel) upshear right (UR), downshear right (DR), downshear left (DL), and upshear left (UL) denoted for each storm. Data are from a 3-h period centered on the times shown in Fig. 3, within the maximum range of eyewall convection from TC center (see Table 1). The bin resolution is 2.5 dBZ in Z_H and 30° in azimuth, with all bin values normalized relative to the maximum value found in any bin of each plot. Superimposed on the density diagrams are average Z_{DR} (red lines; every 0.25 dB at increasing thickness) and K_{DP} (blue lines; every 0.25° km^{-1} at increasing thickness) of the data points falling within each bin. Signatures consistent with the presence of large raindrops (elevated Z_H and Z_{DR}) are indicated by the yellow arrows and those consistent with a high concentration of small drops (elevated Z_H and K_{DP}) by the blue arrows for select storms, pointing to the maximum Z_{DR} and K_{DP} values.

apparent in the weakest and least organized/symmetric storms (Hurricanes Hermine and Nate) and gradually fades in all storms as they weaken (not shown). When considering the remaining storms in order of increasing intensity at these analysis times (i.e., Florence, Arthur, Matthew, Harvey, Irma, and Michael), the size sorting signature becomes more apparent with increasing intensity (see also section 3c and Fig. 4). Namely, the Z_{DR} and K_{DP} enhancements become larger in magnitude and are found over a larger range in azimuth. Environmental wind shear is also found to have a relationship with the azimuthal location of these size sorting signatures. The ERA-Interim 850–200 hPa shear vectors for each TC are superimposed in all maps of Fig. 3, demonstrating that the size sorting signature is observed in a largely consistent shear-relative location within each storm–in the downshear and left-of-shear sectors. These shear-relative locations of size sorting are consistent with prior research on the typical locations of the strongest eyewall convection in TCs experiencing moderate

Brought to you by NOAA Central Library | Unauthenticated | Downloaded 01/14/21 02:34 PM UTC

TABLE 2. For each TC analyzed, the fraction (%) of radar echo that is classified as convective precipitation using the SL3D algorithm. Fractions are provided for each shear-relative quadrant [upshear right (UR), downshear right (DR), downshear left (DL), and upshear left (UL)] and for all echoes, within the maximum range of eyewall convection (see Table 1).

Hurricane	UR	DR	DL	UL	All
Arthur	17.3	21.6	4.0	6.7	12.6
Hermine	8.9	16.4	12.8	9.9	11.7
Matthew	1.2	23.1	19.3	7.7	14.8
Harvey	3.7	1.9	46.6	37.8	21.9
Irma	4.2	39.3	35.8	7.9	25.0
Nate	0.0	10.7	14.8	10.9	13.4
Florence	8.9	2.8	23.5	19.7	13.6
Michael	13.0	19.6	37.9	31.6	25.1

(5–10 m s^{-1}) or strong (>10 m s^{-1}) environmental wind shear (as outlined in section 1; e.g., Corbosiero and Molinari 2002, 2003; Chen et al. 2006; DeHart et al. 2014).

c. *Lower-tropospheric density plot analyses of hydrometeor size sorting*

The influence of size sorting of raindrops within the eyewall convection and its dependence on TC intensity can be more convincingly (and quantitatively) revealed through simple time-composite evaluation. Figure 4 shows two-dimensional frequency (or density) plots of Z_H as a function of 850–200 hPa shear vector-relative azimuth for all 5-min radar observations below 4 km MSL and within a 3-h window centered on the times shown in Fig. 3. Superimposed on these density plots are contours indicating the average values of Z_{DR} and K_{DP} for observations in each Z_H–azimuth bin. It is clear from this more extensive composite analysis that the size sorting signature is more prevalent—with greater magnitudes, azimuthal extents, and azimuthal offsets of Z_{DR} and K_{DP} enhancements within high-Z_H regions found in stronger storms. In particular, azimuthal offsets in Z_{DR} and K_{DP} maxima within $Z_H \geq 40$ dBZ are approximately 90° in Matthew, Harvey, Irma, and Michael, at most 60° in weaker storms and nearly or entirely indistinguishable in Hermine and Florence (both of which are in relatively weak shear environments). Similarly, maximum Z_{DR} and K_{DP} exceed 1.5 dB and 1.25° km^{-1}, respectively, in the stronger storms, but largely fail to exceed 1 dB and 1° km^{-1} in weaker storms. This analysis also demonstrates that Z_{DR} enhancements are commonly found in the downshear quadrants of the eyewall, while the greatest K_{DP} enhancements are commonly found in the left-of-shear quadrants. These shear-relative preferences are also least apparent in the weaker storms. Additionally, diagnosed convection analyzed for the same time period and radii from the TC center (Table 2) demonstrates well that convective precipitation is more prevalent in the stronger TCs.

d. *Time–height analyses*

QVP analysis is possible for only a subset of the TCs analyzed in this study, as construction of such profiles requires that the center of the TC comes in close proximity (within ~50 km) of a NEXRAD WSR-88D site such that the inner core is well sampled. Hurricanes Hermine, Harvey, and Irma each have sufficient observations for QVP analyses, which show consistent physical characteristics of precipitation in the outer rainbands and inner core. Because QVP analysis of Harvey and Irma is possible for an entire 24-h period without interruption in observations, we focus on these storms here. Figure 5 presents time–height curtains of all four radar variables from the QVP analysis of Harvey and Irma. In each case, time series of the location (azimuth) and distance of the radar site used to the TC center and the direction of the 850–200 hPa shear vector are also provided. The locations of the corresponding radars where these QVPs were generated are shown in a storm-relative frame within the lower-tropospheric Z_H maps of Fig. 3. Figure 5 reveals several clear polarimetric signatures within each TC: upward melting-layer displacement within the inner "warm" core compared to that within outer rainbands, a dendritic ice crystal growth layer (DGL—revealed by enhanced Z_{DR} and K_{DP} in environments near −15°C, which are found between 7.5 and 8 km MSL for all TCs analyzed here; e.g., see Kennedy and Rutledge 2011; Andrić et al. 2013; Bechini et al. 2013) spanning altitudes ~1–3 km above the melting layer (illustrated by the blue ovals), and snow aggregation in a shallow layer immediately above the melting layer (revealed by decreasing Z_{DR} and increasing Z_H with decreasing altitude; e.g., see Ryzhkov and Zrnić 1998; Ryzhkov et al. 2005a).

Previous studies have established that there are prominent signatures of hydrometeor melting in the polarimetric variables. Such signatures are typical of hydrometeors falling within broad stratiform rain regions and include the so-called Z_H bright band (a shallow layer of enhanced Z_H) and ρ_{HV} reduction, which are some of the most pronounced polarimetric signatures of melting (e.g., Austin and Bemis 1950; Zrnić et al. 1993; Ryzhkov and Zrnić 1998). These signatures arise as a result of large variability in the shapes, orientations, and phase of melting snow aggregates within stratiform rain regions and from the differences in dielectric constants of liquid and ice. They appear just below the altitude at which melting begins—where the wet bulb temperature in the environment exceeds 0°C.

In Fig. 5, the upward displacement in the melting layer is evidenced by rising altitudes of Z_H and Z_{DR} bright bands and ρ_{HV} reductions over time in each case. For Harvey, these upward displacements are approximately 500 m, and for Irma, approximately 750 m. In both TCs, melting-layer displacements become increasingly defined with decreasing storm-relative distance and are centered near an altitude of 5 km. In Harvey, the rise in melting-layer height is more gradual, occurring over a period of ~6 h and is centered on a distance of ~100 km from storm center. In Irma, the more pronounced rise is more rapid, occurring over a period of ~2 h and centered on a distance of ~150 km from the storm center. These differences in the times during which displacements are seen are likely related to the radar-relative translation speed of the TCs or TC size and the nearest range to TC center sampled. Taken together with the lower-tropospheric maps of Figs. 2 and 3, the distances from storm center where the largest changes are

Brought to you by NOAA Central Library | Unauthenticated | Downloaded 01/14/21 02:34 PM UTC

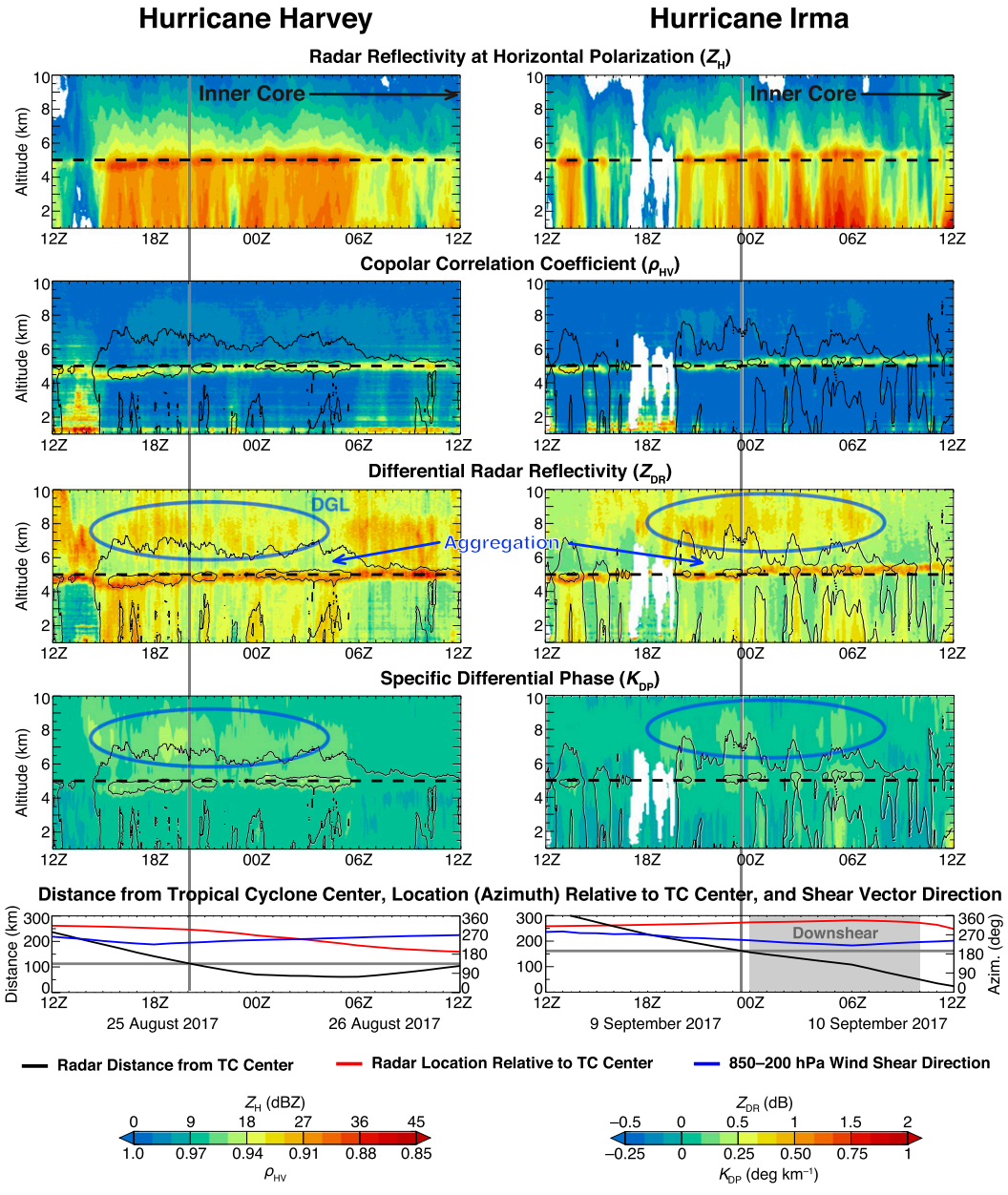

FIG. 5. QVP analyses of Hurricanes (left) Harvey and (right) Irma. (from top to bottom) Time–height curtains of Z_H, ρ_{HV}, Z_{DR}, and K_{DP}, and time series of the distance between the radar location and the TC center (black line), the location of the radar relative to TC center (azimuth in °E of N, red line), and the direction (azimuth) of the 850–200 hPa wind shear vector (blue line). QVPs were created using data from the 12.5° elevation scan in volumes obtained by the Corpus Christi, TX, radar (KCRP) for Hurricane Harvey, and from the 19.5° elevation scan in volumes obtained by the Key West, FL, radar (KBYX) for Hurricane Irma. Vertical and horizontal gray lines demarcate the approximate time and distance from the TC center, respectively, at which the melting layer was displaced upward in each storm. Gray color-filled regions in the bottom panels indicate time periods when the radar was located downshear of the TC center. Thick dashed black horizontal lines indicate an altitude of 5 km for reference and thin black contours in the ρ_{HV}, Z_{DR}, and K_{DP} panels show Z_H = 15 and 30 dBZ. Signatures consistent with the presence of a dendritic growth layer (DGL) are highlighted by the superimposed blue ellipses and those consistent with aggregation by the blue arrows.

Brought to you by NOAA Central Library | Unauthenticated | Downloaded 01/14/21 02:34 PM UTC

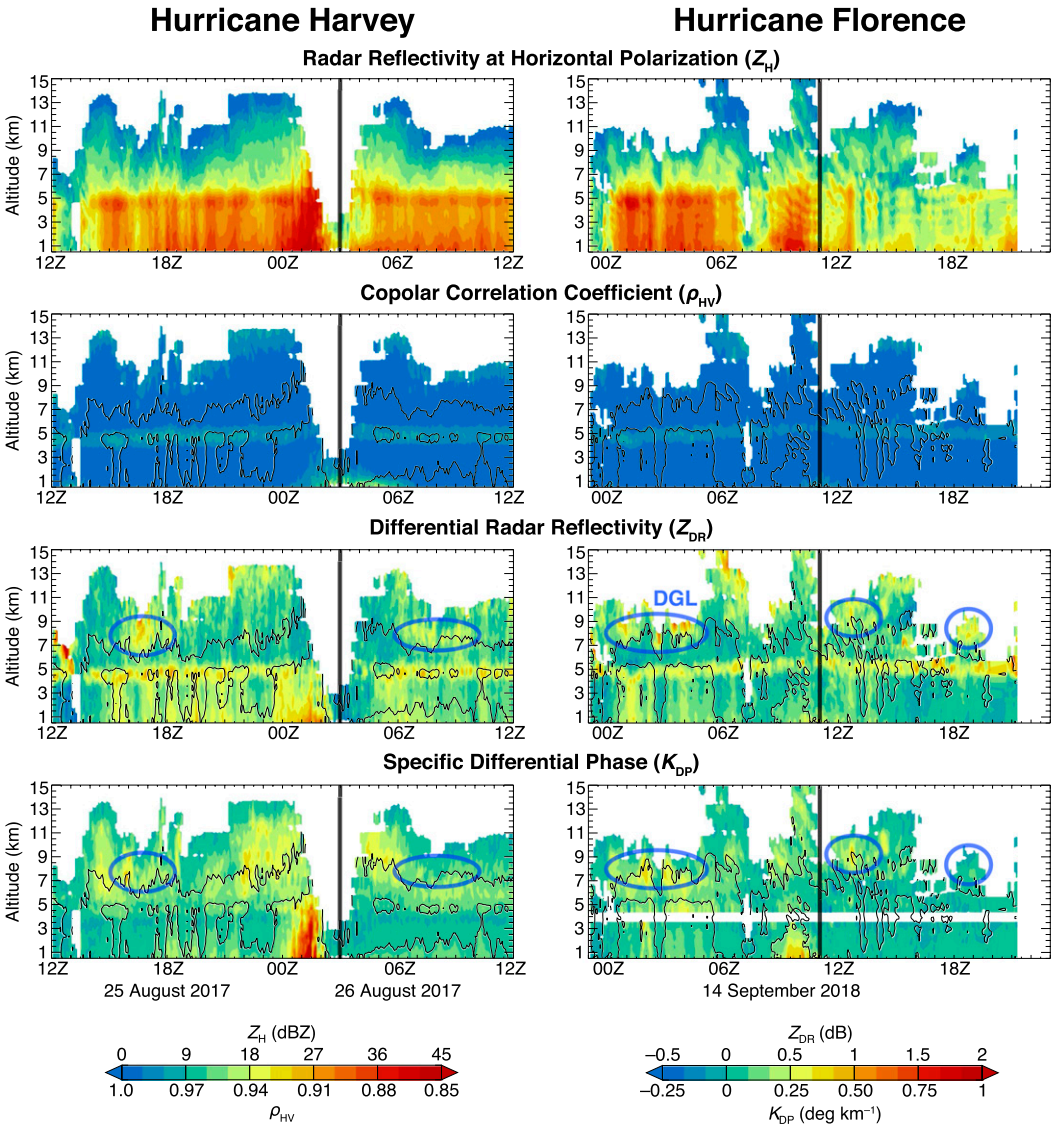

FIG. 6. As in Fig. 5, but for CVP analyses of Hurricanes (left) Harvey and (right) Florence, valid at the same locations as those used for the GridRad time–height curtains included in the online supplement and indicated in Fig. 2. CVPs were created using data from the Corpus Christi, TX, radar (KCRP) for Hurricane Harvey, and from the Wilmington, NC, radar (KLTX) for Hurricane Florence.

observed are consistent with the transition between outer rainbands and inner-core precipitation in each TC [a largely stratiform area referred to as the inner band in Cecil et al. (2002) and Cecil and Zipser (2002)]. Though not shown, this melting-layer displacement in Hermine is also approximately 500 m and coincides with the transition between outer rainbands and inner-core rainband complexes. Hence and Houze (2012) reveal similar offsets in the Z_H bright bands of outer rainbands and inner cores of TCs observed from 10 years of satellite-based radar observations. Didlake and Kumjian (2017) also reveal similar melting-layer displacements within Hurricane Arthur through analysis of profiles of the polarimetric variables from multiple NEXRAD WSR-88D radars. Together, these results reveal the detailed radius-height structure of the TC warm core.

The DGL and aggregation signatures in the QVPs for Harvey and Irma show considerable temporal variability. The variability in the DGL, characterized by periodic enhancements in Z_{DR} and K_{DP} beyond the broad enhancement encompassed within the blue superimposed ellipses in Fig. 5, may indicate evolving mechanisms for ice production (e.g., vertical drafts). Such time-dependent ice production is likely driven in part by variability in convection abundance within outer rainbands and differences near the transition to inner-core precipitation. Overall, these signatures appear to be associated with some of the highest Z_H observed above and below the melting layer, which is consistent with previous studies on winter storms and TCs. In particular, multiple aircraft campaigns targeting TCs have observed large aggregates in the

Brought to you by NOAA Central Library | Unauthenticated | Downloaded 01/14/21 02:34 PM UTC

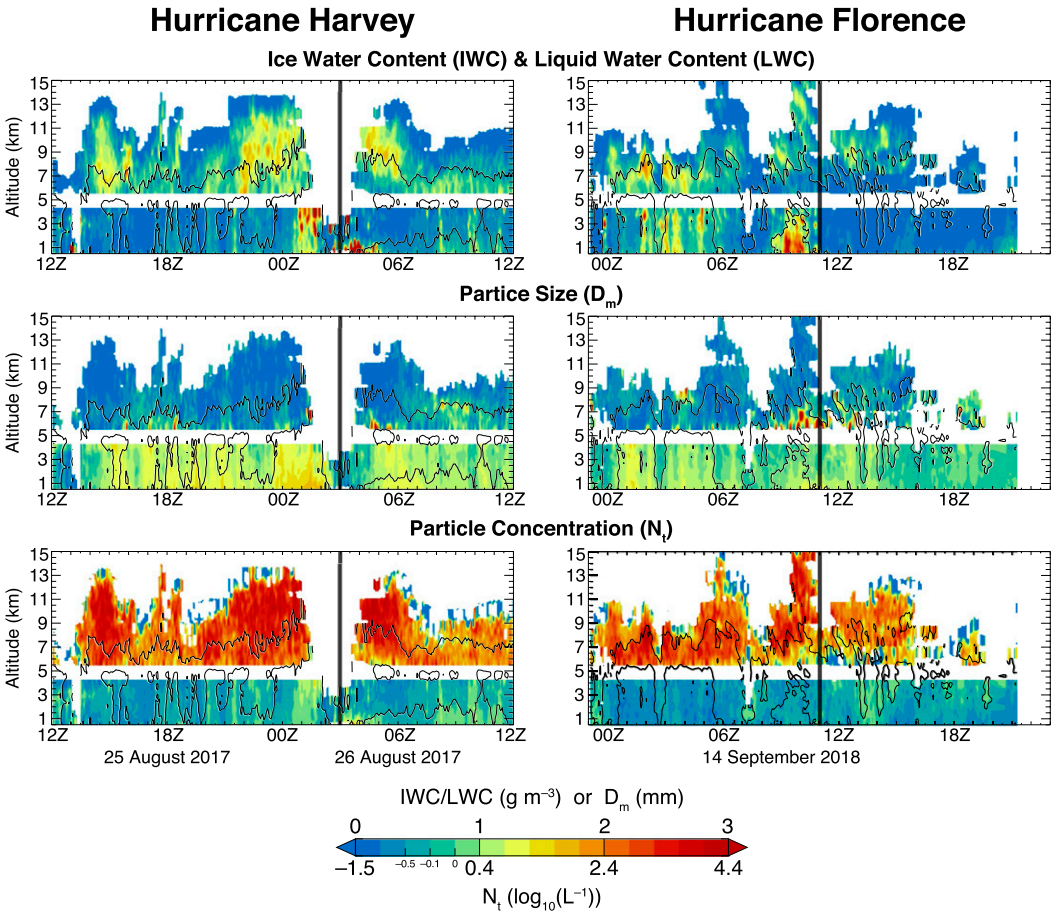

FIG. 7. As in Fig. 6, but for microphysical retrievals of (top) ice water content and liquid water content, (middle) particle size D_m, and (bottom) particle concentration N_t.

inner-core precipitation outside of the eyewall convection (e.g., Houze et al. 1992; Heymsfield et al. 2006).

The final time–height analyses summarized here are rain and ice microphysics retrievals using CVPs from two example TCs–Hurricanes Harvey and Florence (Figs. 6 and 7). The CVPs for Hurricanes Harvey and Florence were created for a 20 km × 20° range–azimuth sector centered on locations that intersect with each TC track, such that the storm passes over the location during the analysis time. Similar time–height curtains of GridRad data for the polarimetric variables only are provided in the supplemental material. Time–height curtains of the polarimetric variables from CVP analysis (Fig. 6) show similar features to those diagnosed in the QVPs, with some minor differences in detail/resolution in the vertical dimension owing to the differences in the two analysis techniques. The corresponding microphysics retrievals (Fig. 7), neglecting data in the melting layer as identified by the radar-observed bright band, provide a more quantitative assessment of precipitation microphysics in TCs and reveal additional detail that is easily overlooked in subjective evaluation of the polarimetric variables alone. Namely, $D_m < 1$ mm and N_t exceeds 1000 L^{-1} nearly everywhere above the melting layer in both TCs, indicating a high concentration of small ice particles aloft. This high concentration of small ice increases competition for available vapor and reduces the likelihood of dendritic growth. However, the microphysics retrievals for the CVPs indicate that signatures of dendritic growth (reduced N_t and increased D_m at altitudes 2–3 km above the melting layer) are found at times when the echo-top altitudes descend to levels near the −15°C isotherm (commonly found at ~8 km MSL; see section 3e and Fig. 10). Signatures of aggregation (increasing D_m and decreasing N_t with decreasing altitude) are also more common at times when dendritic growth is more evident aloft, but such signatures are far weaker than that observed in midlatitude convective systems (e.g., see Fig. 11.12 in Ryzhkov and Zrnić 2019).

Microphysics retrievals below the melting layer, as expected, reveal the dominance of the collision-coalescence warm rain process in TCs, especially in the inner core. Such dominance is evidenced by broadly increasing D_m and LWC with decreasing altitude (driven in the retrievals by strong vertical gradients in Z_H, Z_{DR}, and K_{DP}). One additional notable feature in the CVPs is the slight depression of ρ_{HV} observed between 0100 and 0600 UTC 26 August 2017 in Hurricane Harvey within a

Brought to you by NOAA Central Library | Unauthenticated | Downloaded 01/14/21 02:34 PM UTC

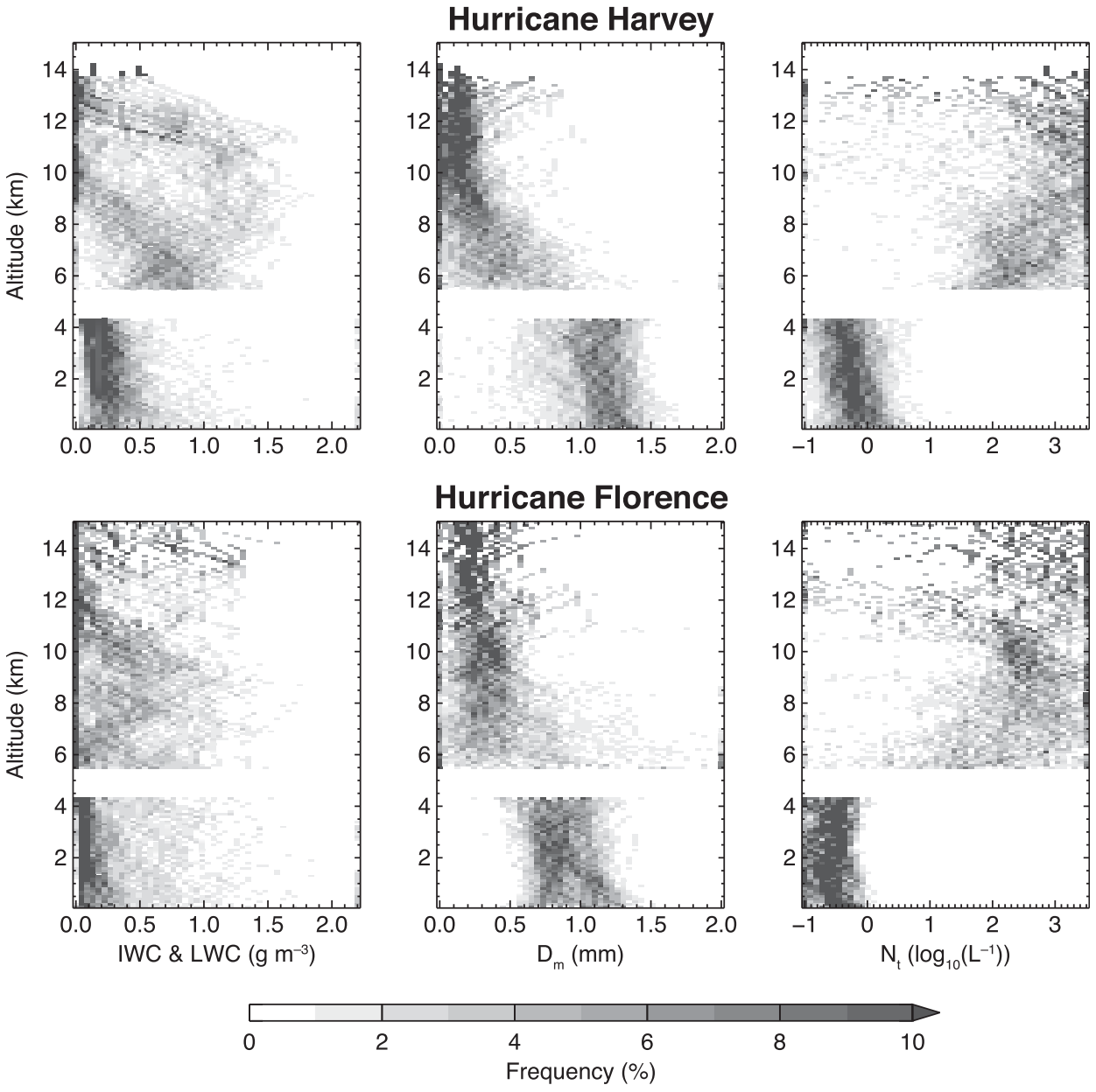

FIG. 8. Contoured frequency by altitude diagrams of the CVP microphysical retrievals in Fig. 7.

~1.5-km-deep layer above ground level. Given that the location of this observation is over the ocean, this signature likely indicates substantial lofting of sea spray by the strong category-4 winds near the storm center at these times. A similar but less apparent reduction of ρ_{HV} is seen near storm center in the CVP for the much weaker Hurricane Florence, which is also located over the ocean.

To facilitate comparison of the CVP microphysics retrieval results with prior studies, contoured frequency by altitude diagrams (CFADs) of the time–height curtains are shown in Fig. 8. The CFADs demonstrate that our estimates of D_m for rain mostly span 1.0 to 1.5 mm for Hurricane Harvey and 0.7 to 1.2 mm for Hurricane Florence, which agree well with the results of DeHart and Bell (2020) (who analyzed the same landfalling TCs, finding a median D_m of ~1.2 mm) and of Wang et al. (2016) and Wen et al. (2018) (for several landfalling TCs in China, finding a mean D_m of ~1.4 mm). Previous studies also typically estimate N_w, a normalized intercept parameter of a gamma DSD instead of the total raindrop concentration N_t. For an exponential DSD, N_t is related to N_w using $N_w = 4N_t/D_m$. Based on the CFADs, N_t varies mostly between −0.8 and 0 in $\log_{10}(L^{-1})$ for the microphysics retrievals here. This translates to an N_w varying between 2.7 and 3.7 in $\log_{10}(m^{-3}\,mm^{-1})$, which is broadly consistent with the value of 3.5 found in Feng and Bell (2019) for the same TCs analyzed here and more than

Brought to you by NOAA Central Library | Unauthenticated | Downloaded 01/14/21 02:34 PM UTC

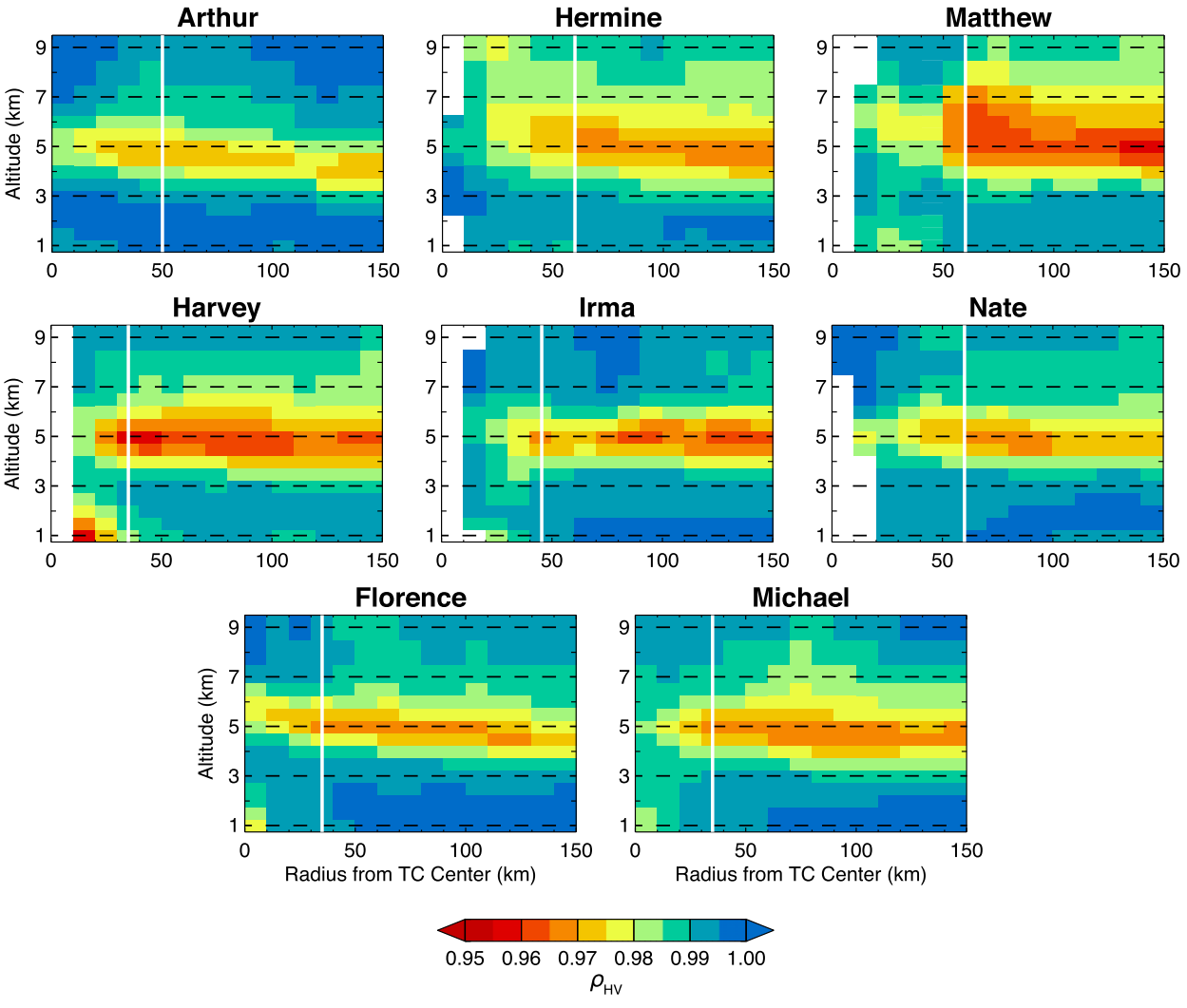

FIG. 9. GridRad average range–height curtains of copolar correlation coefficient (ρ_{HV}) for each TC. As in Fig. 4, data are from a 3-h period centered on the times shown in Fig. 3. Superimposed white lines indicate the maximum range of eyewall convection from the TC center (see Table 1). The bin resolution is 0.5 to 1 km in altitude (the grid spacing of the GridRad data—see section 2a) and 10 km in radius from TC center, with ρ_{HV} values displayed for only those bins that contain at least 100 contributing observations.

an order of magnitude lower than that reported for typhoons in China.

e. *Composite analyses of melting-layer displacements and dendritic growth–layer signatures*

Similar to the density plot analyses used to diagnose lower-tropospheric size sorting signatures within the eyewall convection, we leverage the large volumetric coverage of the GridRad data here to more quantitatively diagnose signatures of melting-layer displacement and dendritic growth via composite analyses. These analyses use data for the same 3-h period as before, centered on the times of the maps in Figs. 2 and 3.

To diagnose melting-layer displacement in each TC using the GridRad data, we collect observations in altitude and distance (radius) from the TC center during the 3-h analysis period. Rather than diagnosing the frequency of such observations, we show the average ρ_{HV} as a function of altitude and radius from the TC center in Fig. 9. Note that this analysis was conducted for each shear-relative quadrant, but no significant differences were found, so we simply show the result for all observations here. This analysis, focused on the inner 150 km of each TC, reveals a different character of melting-layer displacement than that identified in the QVP analysis. Namely, the ρ_{HV} minimum indicative of the melting layer is displaced upward from below 5 km MSL at far ranges to nearly 6 km MSL within 50 km of the TC center, with the greatest inward radial increase in displacement occurring within ~80 km. This upward "bend" in the melting-layer height is somewhat more pronounced in the cohort of weaker TCs, likely driven by a reduced incidence of deep convection within the eyewall (see Table 2). Since the radar bright bands are a prominent stratiform signature, increased convection would bias or even prevent one from diagnosing

Brought to you by NOAA Central Library | Unauthenticated | Downloaded 01/14/21 02:34 PM UTC

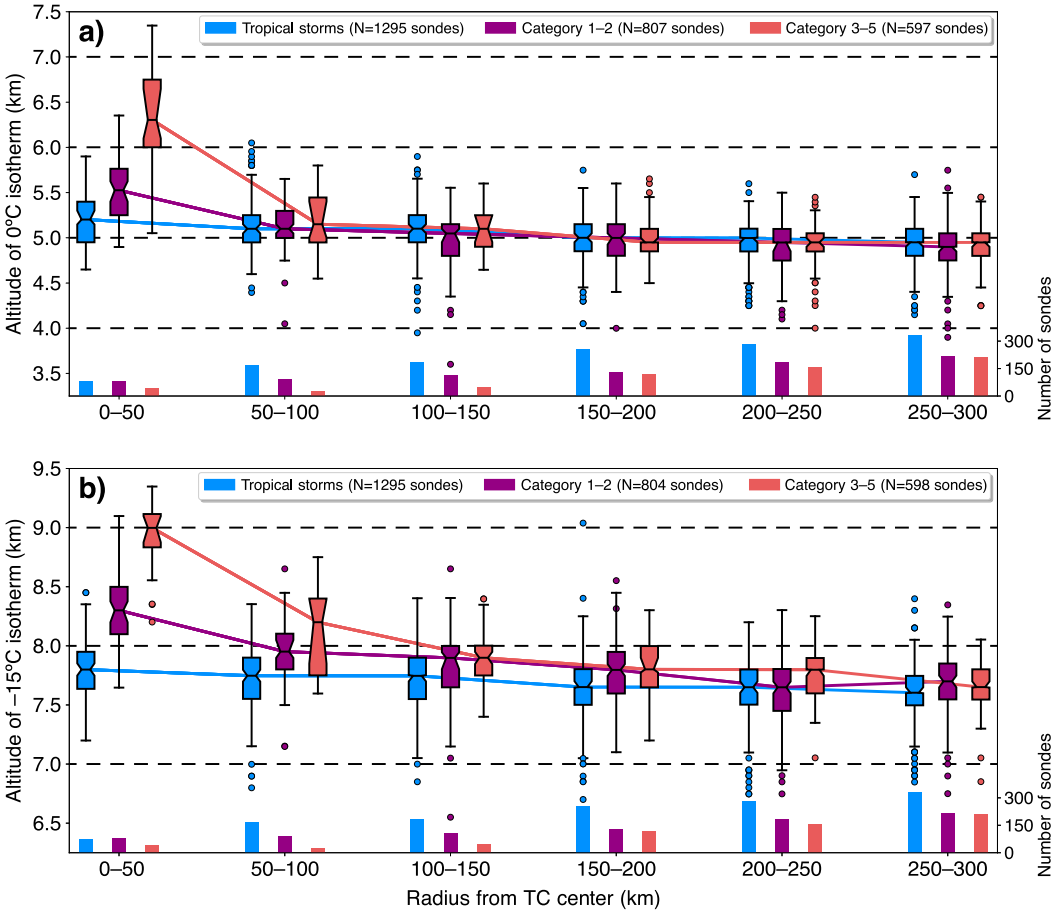

FIG. 10. Radial profile of notched box-and-whisker plots of (a) melting level (km; 0°C isotherm) and (b) dendritic growth level (km; −15°C isotherm) derived from dropsonde data in TCs of Saffir–Simpson intensity: tropical storms (blue), category-1–2 hurricane (purple), and category-3–5 hurricane (red). The number of dropsondes for each radial bin is shown as bar plots along the bottom of the *x*axis. The box plots display the median (vertical lines near box center), the 95% confidence interval of the median calculated from a 1000-sample bootstrap approach with replacement (notches on boxes), the interquartile range (box perimeter; $[q_1, q_3]$), whiskers {horizontal lines extending from box perimeter; $[q_1 - 1.5(q_3 - q_1), q_3 + 1.5(q_3 - q_1)]$}, and outliers (filled circles).

melting-layer height from radar. For the strong TCs analyzed here (Matthew, Harvey, Irma, and Michael), the ρ_{HV} minimum indicative of the melting layer is clearly muted inward of the maximum range of the eyewall convection (illustrated by the white vertical lines in Fig. 9).

For an independent evaluation of the melting-layer displacement and its sensitivity to TC intensity, an analysis of melting-level (0°C) heights determined from several thousand dropsondes in category-3–5 hurricanes, category-1–2 hurricanes, and tropical storms are presented in Fig. 10a. This analysis also clearly demonstrates that melting-level/layer displacements are commonly greatest in strong TCs, particularly within a 50-km radius from the TC center (i.e., within the eyewall convection and cloud-free eye). Thus, despite the fact that melting-level displacements in the inner core can approach 1 km relative to the far-field environment in strong TCs, the increased likelihood that these are within (and partially driven by) convection (e.g., see Table 2) means that radars will not be able to diagnose the melting layer well in this region, which is likely the primary reason why less melting-layer displacement is identified in the stronger TCs analyzed here. The dropsondes also reveal a smaller transition in melting-level height of ~200 m near a radius of ~150 km that is consistent with that identified in the QVPs here.

DGLs are well-revealed in the GridRad data. The time-evolving character of the DGL signatures in each TC from GridRad can be seen in time–height curtains provided in the supplemental material, but here we focus on the unique relationship between DGL occurrence and echo-top altitude identified in the CVP analysis. To demonstrate this more robustly, Fig. 11 shows density diagrams of observed Z_{DR} at an altitude of 8 km MSL (broadly coinciding with the altitude of the −15°C isotherm) as a function of the observed $Z_H = 10$ dBZ echo-top altitude for observations at ranges of up to 200 km and outside of the maximum range of eyewall convection in each TC. The GridRad data are ideal for this

Brought to you by NOAA Central Library | Unauthenticated | Downloaded 01/14/21 02:34 PM UTC

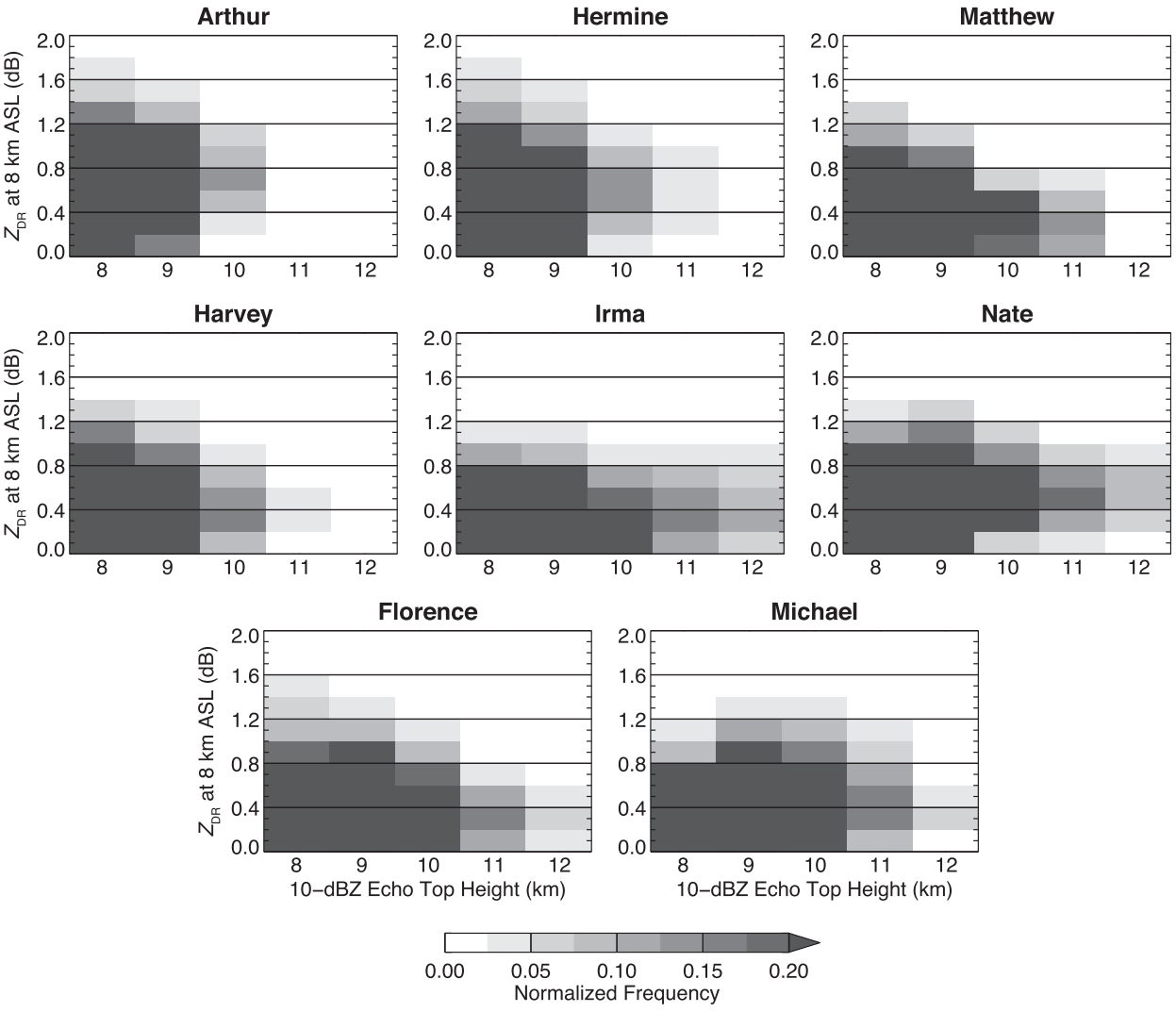

FIG. 11. Two-dimensional density diagrams (or histograms) of GridRad differential radar reflectivity (Z_{DR}) at an altitude of 8 km MSL as a function of $Z_H = 10$ dBZ echo-top altitude for each TC. Data are from a 3-h period centered on the times shown in Fig. 3 and span ranges from the maximum range of eyewall convection (see Table 1) out to 200 km from TC center. The bin resolution is 1 km in echo-top altitude and 0.2 dB in Z_{DR}, with all bin values normalized relative to the maximum value found in any bin of each plot.

type of analysis because the echo-top altitudes diagnosed from GridRad have an uncertainty of ±1 km (comparable to the vertical sampling of overlapping radars) and are unbiased based on comparisons with independent, higher-resolution observations (e.g., Homeyer and Bowman 2017; Cooney et al. 2018). Figure 11 demonstrates that DGLs (evidenced by Z_{DR} near and exceeding 1 dB here, though similar diagrams using K_{DP} are consistent) only routinely appear when the echo-top altitude is nearer the −15°C isotherm (≤10 km).

The tendency for DGLs to be more common when echo-top altitudes are low is consistent with that found in winter storms by Griffin et al. (2018). Such sensitivity to echo-top height is likely indicative of the sensitivity of ice crystal growth to crystal size. When ice crystals are sufficiently small (i.e., shortly after nucleation), their growth and resulting aspect ratio that will determine their radar scattering characteristics will be most sensitive to the temperature and excess vapor in their environment, which dictates the primary habit (i.e., particle shape) they will assume. Thus, when echo-top heights are near the −15°C isotherm (and ice crystals are assumed to be nearer to nucleation size and fewer in concentration) in an environment with significant excess vapor, rapid dendritic growth is most likely. As ice particles increase in size, they will require a greater mass of excess vapor for similar incremental growth in the thermodynamically preferred aspect ratio and significant dendritic growth will be less likely. While shear-relative location is not shown here, we did not find a strong relationship between the occurrence of the DGL and shear-relative location, but DGLs were not found within eyewall convection and were most common within the stratiform regions of the inner core. It should also be noted that the altitude at which a DGL would be found will increase with decreasing radius from the TC center. In particular, the dropsonde analysis in Fig. 10b

Brought to you by NOAA Central Library | Unauthenticated | Downloaded 01/14/21 02:34 PM UTC

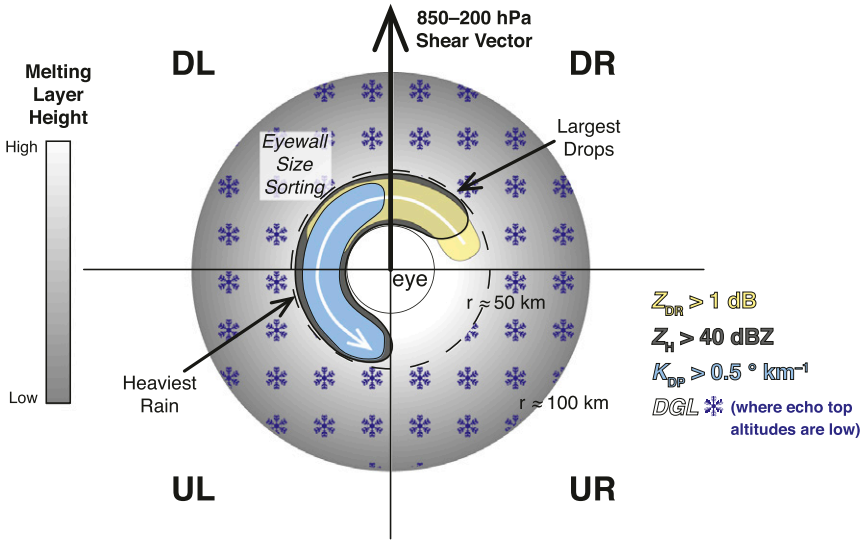

FIG. 12. Conceptual illustration summarizing the polarimetric radar signatures found within the inner core of a tropical cyclone. The radial extent of the inner-core precipitation is given by the light gradient color-filled region, the color of which reflects the radially inward increase in melting-layer (ML) height. The white arrow represents the primary circulation of the TC and the thick black arrow represents the direction of the 850–200 hPa shear vector. Shear-relative quadrants are identified as upshear left (UL), upshear right (UR), downshear right (DR), and downshear left (DL). Blue dendrite symbols highlight stratiform, low echo-top regions where dendritic growth layers (DGL) are found.

shows that the −15°C isotherm often associated with the DGL is displaced slightly more than the melting level with decreasing radius, since temperature anomalies in the warm core increase in magnitude with increasing altitude in the middle and upper troposphere inside and outside of the eye in association with the warm-core storm structure (Hawkins and Rubsam 1968; Frank 1977; Stern and Nolan 2012). This issue is minimized in Fig. 11 by excluding observations within the maximum radius of eyewall convection from the analysis.

4. Summary and discussion

This study documented recently observed polarimetric radar signatures within TCs from an analysis of eight landfalling storms in the CONUS that spanned a broad range of hurricane intensities on the Saffir–Simpson scale. A two-dimensional illustration summarizing these polarimetric signatures is provided in Fig. 12. Observations from the NEXRAD WSR-88D network were used to analyze maps and vertical profiles of the polarimetric variables, which revealed three prominent microphysical signatures that have been diagnosed previously for individual cases:

1) Hydrometeor size sorting within the eyewall convection (Figs. 3 and 4) that is most prevalent in stronger storms and in downshear and left-of-shear storm quadrants (indicated by the yellow and blue shading for high Z_{DR} and high K_{DP}, respectively, in Fig. 12);
2) Upward melting-layer displacement near the transition zone between the outer rainbands and inner-core rainband complex (see Fig. 5) and to a greater extent as the radial distance from the TC center decreases, especially within a radius of 50 km (Figs. 9 and 10a; illustrated by the gray color-fill in Fig. 12); and
3) Indications of dendritic growth and aggregation above the melting layer within stratiform regions of the inner core (Figs. 5–7 and 11; illustrated by dendrite symbols outside of the eyewall in Fig. 12) that are most prevalent when echo-top altitudes are low (≤10 km MSL, nearer the −15°C isotherm often associated with dendritic growth, which is commonly near 8 km in TCs—e.g., see Fig. 10b).

The main novelty of the work summarized here is the investigation of multiple landfalling TCs at varying intensity using polarimetric radar observations. The dependence of the lower-tropospheric size sorting result on TC intensity is particularly notable as previous work revealing this signature had focused on case studies of only a single TC. In addition, the dependence of melting-layer altitude on range from TC center has been well known, but this work has revealed the increase in vertical displacement with increasing TC intensity and the complexity of its identification using polarimetric radar observations. Identification of the melting-layer displacement from radar can help remotely assess the often rapid evolution of TC intensity at landfall and the corresponding warm cloud depth and precipitation potential of landfalling TCs. Finally, the identification of routinely observed DGLs in TCs and their dependence on echo-top altitude is perhaps the most novel result of this work and demonstrates the unique potential of leveraging polarimetric radar observations for characterization of TC microphysics.

The routinely identified microphysical signatures in TCs documented here are of relevance to future observational and

Brought to you by NOAA Central Library | Unauthenticated | Downloaded 01/14/21 02:34 PM UTC

modeling work. While a strength of this analysis was a review of common signatures across multiple landfalling events and at varying TC intensity, more detailed examinations of each storm and their time-evolving microphysical characteristics are necessary, particularly focused on the less examined DGL. Moreover, understanding the evolution of small ice particles growing into larger particles is particularly important for assessing cloud radiative processes, which need to be examined more closely as well given their ties to storm size and intensity evolution. Current numerical models have difficulty reproducing small ice and raindrop size sorting signatures, so validation studies and microphysical parameterization experiments are necessary efforts that must be carried out to improve the models based on emerging polarimetric radar studies of TCs.

Acknowledgments. We thank the anonymous reviewers for providing thoughtful comments that helped improve the manuscript. All graphics in this paper were designed to be equally interpretable for individuals with full color vision and individuals with color vision deficiency. This material is based upon work supported by the National Science Foundation under Grant ICER-1663840 and by the U.S. Department of Energy, Office of Science under Award DE-SC0014295. Auxiliary funding was provided by NOAA/Office of Oceanic and Atmospheric Research under NOAA–University of Oklahoma Cooperative Agreement NA11OAR4320072, U.S. Department of Commerce. Development of the dropsonde dataset is supported by NASA Earth Science Grant 80NSSC19K0012 under the Weather and Dynamics program. This report was prepared as an account of work sponsored by an agency of the U.S. government. Neither the U.S. government nor any agency thereof, nor any of their employees, makes any warranty, express or implied, or assumes any legal liability or responsibility for the accuracy, or represents that its use would not infringe privately owned rights. Reference herein to any specific commercial product, process, or service by trade name, trademark, manufacturer, or otherwise does not necessarily constitute or imply its endorsement, recommendation, or favoring by the U.S. government or any agency thereof. The views and opinions of authors expressed herein do not necessarily state or reflect those of the U.S. government or any agency thereof.

Data availability statement. The radar observations, model output, and TC track data used in this study are freely available online in archives hosted by the National Centers for Environmental Information (NCEI; the NEXRAD WSR-88D data), the European Centre for Medium-Range Weather Forecasts (ECMWF; the ERA-Interim reanalysis), NOAA's Atlantic Oceanographic and Meteorological Laboratory/Hurricane Research Division (the dropsonde data), and the National Hurricane Center (NHC; the HURDAT2 TC tracks). All processed datasets produced by the authors for this study are available upon request.

REFERENCES

Andrić, J., M. R. Kumjian, D. S. Zrnić, J. M. Straka, and V. M. Melnikov, 2013: Polarimetric signatures above the melting layer in winter storms: An observational and modeling study. *J. Appl. Meteor. Climatol.*, **52**, 682–700, https://doi.org/10.1175/JAMC-D-12-028.1.

Austin, P. M., and A. C. Bemis, 1950: A quantitative study of the "bright band" in radar precipitation echoes. *J. Meteor.*, **7**, 145–151, https://doi.org/10.1175/1520-0469(1950)007<0145:AQSOTB>2.0.CO;2.

Bechini, R., L. Baldini, and V. Chandrasekar, 2013: Polarimetric radar observations in the ice region of precipitating clouds at C-band and X-band radar frequencies. *J. Appl. Meteor. Climatol.*, **52**, 1147–1169, https://doi.org/10.1175/JAMC-D-12-055.1.

Black, M. L., J. F. Gamache, F. D. Marks, C. E. Samsury, and H. E. Willoughby, 2002: Eastern Pacific Hurricanes Jimena of 1991 and Olivia of 1994: The effect of vertical shear on structure and intensity. *Mon. Wea. Rev.*, **130**, 2291–2312, https://doi.org/10.1175/1520-0493(2002)130<2291:EPHJOA>2.0.CO;2.

Black, R. A., 1984: Distribution of particle types above 6.0 km in two Atlantic hurricanes. *16th Conf. on Hurricanes and Tropical Meteorology*, San Diego, CA, Amer. Meteor. Soc., 537–541.

——, and J. Hallett, 1986: Observations of the distribution of ice in hurricanes. *J. Atmos. Sci.*, **43**, 802–822, https://doi.org/10.1175/1520-0469(1986)043<0802:OOTDOI>2.0.CO;2.

Bosart, L. F., C. S. Velden, W. E. Bracken, J. Molinari, and P. G. Black, 2000: Environmental influences on the rapid intensification of Hurricane Opal (1995) over the Gulf of Mexico. *Mon. Wea. Rev.*, **128**, 322–352, https://doi.org/10.1175/1520-0493(2000)128<0322:EIOTRI>2.0.CO;2.

Bowman, K. P., and C. R. Homeyer, 2017: GridRad—Three-dimensional gridded NEXRAD WSR-88D radar data. The National Center for Atmospheric Research, Computational and Information Systems Laboratory, accessed 1 November 2019, https://doi.org/10.5065/D6NK3CR7.

Brandes, E. A., K. Ikeda, G. Zhang, M. Schönhuber, and R. M. Rasmussen, 2007: A statistical and physical description of hydrometeor distributions in Colorado snowstorms using a video disdrometer. *J. Appl. Meteor. Climatol.*, **46**, 634–650, https://doi.org/10.1175/JAM2489.1.

Brauer, N. S., J. B. Basara, C. R. Homeyer, G. M. McFarquhar, and P. E. Kirstetter, 2020: Quantifying precipitation efficiency and drivers of excessive precipitation in post-landfall Hurricane Harvey. *J. Hydrometeor.*, **21**, 433–452, https://doi.org/10.1175/JHM-D-19-0192.1.

Braun, S. A., and L. Wu, 2007: A numerical study of Hurricane Erin (2001). Part II: Shear and the organization of eyewall vertical motion. *Mon. Wea. Rev.*, **135**, 1179–1194, https://doi.org/10.1175/MWR3336.1.

Bringi, V. N., and V. Chandrasekar, 2001: *Polarimetric Doppler Weather Radar*. 1st ed. Cambridge University Press, 636 pp.

Brown, B. R., M. M. Bell, and A. J. Frambach, 2016: Validation of simulated hurricane drop size distributions using polarimetric radar. *Geophys. Res. Lett.*, **43**, 910–917, https://doi.org/10.1002/2015GL067278.

Cecil, D. J., and E. J. Zipser, 2002: Reflectivity, ice scattering, and lightning characteristics of hurricane eyewalls and rainbands. Part II: Intercomparison of observations. *Mon. Wea. Rev.*, **130**, 785–801, https://doi.org/10.1175/1520-0493(2002)130<0785:RISALC>2.0.CO;2.

——, ——, and S. W. Nesbitt, 2002: Reflectivity, ice scattering, and lightning characteristics of hurricane eyewalls and rainbands. Part I: Quantitative description. *Mon. Wea. Rev.*, **130**, 769–784, https://doi.org/10.1175/1520-0493(2002)130<0769:RISALC>2.0.CO;2.

Chen, H., and D.-L. Zhang, 2013: On the rapid intensification of Hurricane Wilma (2005). Part II: Convective bursts and the

Brought to you by NOAA Central Library | Unauthenticated | Downloaded 01/14/21 02:34 PM UTC

upper-level warm core. *J. Atmos. Sci.*, **70**, 146–162, https://doi.org/10.1175/JAS-D-12-062.1.

Chen, S. S., J. A. Knaff, and F. D. Marks, 2006: Effects of vertical wind shear and storm motion on tropical cyclone rainfall asymmetries deduced from TRMM. *Mon. Wea. Rev.*, **134**, 3190–3208, https://doi.org/10.1175/MWR3245.1.

Cooney, J. W., K. P. Bowman, C. R. Homeyer, and T. M. Fenske, 2018: Ten-year analysis of tropopause-overshooting convection using gridrad data. *J. Geophys. Res. Atmos.*, **123**, 329–343, https://doi.org/10.1002/2017JD027718.

Corbosiero, K. L., and J. Molinari, 2002: The effects of vertical wind shear on the distribution of convection in tropical cyclones. *Mon. Wea. Rev.*, **130**, 2110–2123, https://doi.org/10.1175/1520-0493(2002)130<2110:TEOVWS>2.0.CO;2.

——, and ——, 2003: The relationship between storm motion, vertical wind shear, and convective asymmetries in tropical cyclones. *J. Atmos. Sci.*, **60**, 366–376, https://doi.org/10.1175/1520-0469(2003)060<0366:TRBSMV>2.0.CO;2.

Crum, T. D., and R. L. Alberty, 1993: The WSR-88D and the WSR-88D operational support facility. *Bull. Amer. Meteor. Soc.*, **74**, 1669–1687, https://doi.org/10.1175/1520-0477(1993)074<1669:TWATWO>2.0.CO;2.

Dee, D. P., and Coauthors, 2011: The ERA-Interim reanalysis: Configuration and performance of the data assimilation system. *Quart. J. Roy. Meteor. Soc.*, **137**, 553–597, https://doi.org/10.1002/qj.828.

DeHart, J. C., and M. M. Bell, 2020: A comparison of the polarimetric radar characteristics of heavy rainfall from Hurricanes Harvey (2017) and Florence (2018). *J. Geophys. Res. Atmos.*, **125**, e2019JD032212, https://doi.org/10.1029/2019JD032212.

——, R. A. Houze, and R. F. Rogers, 2014: Quadrant distribution of tropical cyclone inner-core kinematics in relation to environmental shear. *J. Atmos. Sci.*, **71**, 2713–2732, https://doi.org/10.1175/JAS-D-13-0298.1.

DeMaria, M., 1996: The effect of vertical wind shear on tropical cyclone intensity change. *J. Atmos. Sci.*, **53**, 2076–2088, https://doi.org/10.1175/1520-0469(1996)053<2076:TEOVSO>2.0.CO;2.

——, C. R. Sampson, J. A. Knaff, and K. D. Musgrave, 2014: Is tropical cyclone intensity guidance improving? *Bull. Amer. Meteor. Soc.*, **95**, 387–398, https://doi.org/10.1175/BAMS-D-12-00240.1.

Didlake, A. C., and M. R. Kumjian, 2017: Examining polarimetric radar observations of bulk microphysical structures and their relation to vortex kinematics in Hurricane Arthur (2014). *Mon. Wea. Rev.*, **145**, 4521–4541, https://doi.org/10.1175/MWR-D-17-0035.1.

——, and ——, 2018: Examining storm asymmetries in Hurricane Irma (2017) using polarimetric radar observations. *Geophys. Res. Lett.*, **45**, 13 513–13 522, https://doi.org/10.1029/2018GL080739.

Doviak, R. J., and D. S. Zrnić, 1993: *Doppler Radar and Weather Observations*. 2nd ed. Dover Publications, Inc., 562 pp.

Dunion, J. P., G. A. Wick, P. G. Black, and J. Walker, 2018: Sensing hazards with operational unmanned technology: 2015–2016 campaign summary, final report. NOAA Tech. Memo. OAR UAS-001, 49 pp., https://uas.noaa.gov/Portals/5/Docs/NOAA-UAS-Tech-Memo-1-SHOUT-Field-Campaigns-Summary_25Apr2018.pdf.

Eastin, M. D., W. M. Gray, and P. G. Black, 2005: Buoyancy of convective vertical motions in the inner core of intense hurricanes. Part II: Case studies. *Mon. Wea. Rev.*, **133**, 209–227, https://doi.org/10.1175/MWR-2849.1.

Emory, A. E., M. McLinden, M. Schreier, and G. A. Wick, 2015: An introduction to the NASA East Pacific Origins and Characteristics of Hurricanes (EPOCH) field campaign. *Trop. Cyclone Res. Rev.*, 124–131, https://doi.org/10.6057/2015TCRRh3.03.

Feng, Y.-C., and M. M. Bell, 2019: Microphysical characteristics of an asymmetric eyewall in major Hurricane Harvey (2017). *Geophys. Res. Lett.*, **46**, 461–471, https://doi.org/10.1029/2018GL080770.

Fierro, A. O., and E. R. Mansell, 2017: Electrification and lightning in idealized simulations of a hurricane-like vortex subject to wind shear and sea surface temperature cooling. *J. Atmos. Sci.*, **74**, 2023–2041, https://doi.org/10.1175/JAS-D-16-0270.1.

——, R. F. Rogers, F. D. Marks, and D. S. Nolan, 2009: The impact of horizontal grid spacing on the microphysical and kinematic structures of strong tropical cyclones simulated with the WRF-ARW model. *Mon. Wea. Rev.*, **137**, 3717–3743, https://doi.org/10.1175/2009MWR2946.1.

Fischer, M. S., R. F. Rogers, and P. D. Reasor, 2020: The rapid intensification and eyewall replacement cycles of Hurricane Irma (2017). *Mon. Wea. Rev.*, **148**, 981–1004, https://doi.org/10.1175/MWR-D-19-0185.1.

Frank, W. M., 1977: The structure and energetics of the tropical cyclone. Part I: Storm structure. *Mon. Wea. Rev.*, **105**, 1119–1135, https://doi.org/10.1175/1520-0493(1977)105<1119:TSAEOT>2.0.CO;2.

——, and E. A. Ritchie, 1999: Effects of environmental flow upon tropical cyclone structure. *Mon. Wea. Rev.*, **127**, 2044–2061, https://doi.org/10.1175/1520-0493(1999)127<2044:EOEFUT>2.0.CO;2.

Franklin, J. L., S. J. Lord, S. E. Feuer, and F. D. Marks, 1993: The kinematic structure of Hurricane Gloria (1985) determined from nested analyses of dropwindsonde and Doppler radar data. *Mon. Wea. Rev.*, **121**, 2433–2451, https://doi.org/10.1175/1520-0493(1993)121<2433:TKSOHG>2.0.CO;2.

Gall, R., J. Franklin, F. Marks, E. N. Rappaport, and F. Toepfer, 2013: The Hurricane Forecast Improvement Project. *Bull. Amer. Meteor. Soc.*, **94**, 329–343, https://doi.org/10.1175/BAMS-D-12-00071.1.

Gamache, J. F., H. E. Willoughby, M. L. Black, and C. E. Samsury, 1997: Wind shear, sea surface temperature and convection in hurricanes observed by airborne Doppler radar. *22nd Conf. on Hurricanes and Tropical Meteorology*, Fort Collins, CO, Amer. Meteor. Soc., 121–122.

Gray, W. M., 1968: Global view of the origin of tropical disturbances and storms. *Mon. Wea. Rev.*, **96**, 669–700, https://doi.org/10.1175/1520-0493(1968)096<0669:GVOTOO>2.0.CO;2.

Griffin, E. M., T. J. Schuur, D. R. MacGorman, M. R. Kumjian, and A. O. Fierro, 2014: An electrical and polarimetric analysis of the overland reintensification of Tropical Storm Erin (2007). *Mon. Wea. Rev.*, **142**, 2321–2344, https://doi.org/10.1175/MWR-D-13-00360.1.

——, ——, and A. V. Ryzhkov, 2018: A polarimetric analysis of ice microphysical processes in snow, using quasi-vertical profiles. *J. Appl. Meteor. Climatol.*, **57**, 31–50, https://doi.org/10.1175/JAMC-D-17-0033.1.

Guimond, S. R., G. M. Heymsfield, and F. J. Turk, 2010: Multiscale observations of Hurricane Dennis (2005): The effects of hot towers on rapid intensification. *J. Atmos. Sci.*, **67**, 633–654, https://doi.org/10.1175/2009JAS3119.1.

Gunn, R., and G. D. Kinser, 1949: The terminal velocity of fall for water droplets in stagnant air. *J. Meteor.*, **6**, 243–248, https://doi.org/10.1175/1520-0469(1949)006<0243:TTVOFF>2.0.CO;2.

Hallett, J., and S. C. Mossop, 1974: Production of secondary ice particles during the riming process. *Nature*, **249**, 26–28, https://doi.org/10.1038/249026a0.

Brought to you by NOAA Central Library | Unauthenticated | Downloaded 01/14/21 02:34 PM UTC

Handler, S. L., and C. R. Homeyer, 2018: Radar-observed bulk microphysics of midlatitude leading line trailing stratiform mesoscale convective systems. *J. Appl. Meteor. Climatol.*, **57**, 2231–2248, https://doi.org/10.1175/JAMC-D-18-0030.1.

Hanley, D., J. Molinari, and D. Keyser, 2001: A composite study of the interactions between tropical cyclones and upper-tropospheric troughs. *Mon. Wea. Rev.*, **129**, 2570–2584, https://doi.org/10.1175/1520-0493(2001)129<2570:ACSOTI>2.0.CO;2.

Hawkins, H., and D. Rubsam, 1968: Hurricane Hilda, 1964. *Mon. Wea. Rev.*, **96**, 617–636, https://doi.org/10.1175/1520-0493(1968)096<0617:HH>2.0.CO;2.

Hazelton, A. T., R. Rogers, and R. E. Hart, 2015: Shear-relative asymmetries in tropical cyclone eyewall slope. *Mon. Wea. Rev.*, **143**, 883–903, https://doi.org/10.1175/MWR-D-14-00122.1.

——, R. E. Hart, and R. F. Rogers, 2017: Analyzing simulated convective bursts in two Atlantic hurricanes. Part II: Intensity change due to bursts. *Mon. Wea. Rev.*, **145**, 3095–3117, https://doi.org/10.1175/MWR-D-16-0268.1.

Hence, D. A., and R. A. Houze, 2011: Vertical structure of hurricane eyewalls as seen by the TRMM Precipitation Radar. *J. Atmos. Sci.*, **68**, 1637–1652, https://doi.org/10.1175/2011JAS3578.1.

——, and ——, 2012: Vertical structure of tropical cyclone rainbands as seen by the TRMM Precipitation Radar. *J. Atmos. Sci.*, **69**, 2644–2661, https://doi.org/10.1175/JAS-D-11-0323.1.

Hendricks, E. A., M. T. Montgomery, and C. A. Davis, 2004: The role of "vortical" hot towers in the formation of Tropical Cyclone Diana (1984). *J. Atmos. Sci.*, **61**, 1209–1232, https://doi.org/10.1175/1520-0469(2004)061<1209:TROVHT>2.0.CO;2.

——, M. S. Peng, X. Ge, and T. Li, 2011: Performance of a dynamic initialization scheme in the Coupled Ocean–Atmosphere Mesoscale Prediction System for Tropical Cyclones (COAMPS-TC). *Wea. Forecasting*, **26**, 650–663, https://doi.org/10.1175/WAF-D-10-05051.1.

Herzegh, P. H., and A. R. Jameson, 1992: Observing precipitation through dual-polarization radar measurements. *Bull. Amer. Meteor. Soc.*, **73**, 1365–1374, https://doi.org/10.1175/1520-0477(1992)073<1365:OPTDPR>2.0.CO;2.

Heymsfield, A. J., A. Bansemer, S. L. Durden, R. L. Herman, and T. P. Bui, 2006: Ice microphysics observations in Hurricane Humberto: Comparison with non-hurricane-generated ice cloud layers. *J. Atmos. Sci.*, **63**, 288–308, https://doi.org/10.1175/JAS3603.1.

Homeyer, C. R., and M. R. Kumjian, 2015: Microphysical characteristics of overshooting convection from polarimetric radar observations. *J. Atmos. Sci.*, **72**, 870–891, https://doi.org/10.1175/JAS-D-13-0388.1.

——, and K. P. Bowman, 2017: Algorithm description document for version 3.1 of the three-dimensional Gridded NEXRAD WSR-88D Radar (GridRad) dataset. Tech. Rep., 23 pp., https://gridrad.org/pdf/GridRad-v3.1-Algorithm-Description.pdf.

Houze, R. A., 2010: Clouds in tropical cyclones. *Mon. Wea. Rev.*, **138**, 293–344, https://doi.org/10.1175/2009MWR2989.1.

——, F. D. Marks, and R. A. Black, 1992: Dual-aircraft investigation of the inner core of Hurricane Norbert. Part II: Mesoscale distribution of ice particles. *J. Atmos. Sci.*, **49**, 943–963, https://doi.org/10.1175/1520-0469(1992)049<0943:DAIOTI>2.0.CO;2.

Hu, J., D. Rosenfeld, A. Ryzhkov, and P. Zhang, 2020: Synergetic use of the WSR-88D radars, GOES-R satellites, and lightning networks to study microphysical characteristics of hurricanes. *J. Appl. Meteor. Climatol.*, **59**, 1051–1068, https://doi.org/10.1175/JAMC-D-19-0122.1.

Hubbert, J. C., V. N. Bringi, L. D. Carey, and S. Bolen, 1998: CSU–CHILL polarimetric radar measurements from a severe hail storm in eastern Colorado. *J. Appl. Meteor.*, **37**, 749–775, https://doi.org/10.1175/1520-0450(1998)037<0749:CCPRMF>2.0.CO;2.

Jones, S. C., 1995: The evolution of vortices in vertical shear. I: Initially barotropic vortices. *Quart. J. Roy. Meteor. Soc.*, **121**, 821–851, https://doi.org/10.1002/qj.49712152406.

Jorgensen, D. P., E. J. Zipser, and M. A. LeMone, 1985: Vertical motions in intense hurricanes. *J. Atmos. Sci.*, **42**, 839–856, https://doi.org/10.1175/1520-0469(1985)042<0839:VMIIH>2.0.CO;2.

Kaplan, J., and M. DeMaria, 2003: Large-scale characteristics of rapidly intensifying tropical cyclones in the North Atlantic basin. *Wea. Forecasting*, **18**, 1093–1108, https://doi.org/10.1175/1520-0434(2003)018<1093:LCORIT>2.0.CO;2.

Kennedy, P. C., and S. A. Rutledge, 2011: S-band dual-polarization radar observations of winter storms. *J. Appl. Meteor. Climatol.*, **50**, 844–858, https://doi.org/10.1175/2010JAMC2558.1.

Kossin, J. P., and M. DeMaria, 2016: Reducing operational hurricane intensity forecast errors during eyewall replacement cycles. *Wea. Forecasting*, **31**, 601–608, https://doi.org/10.1175/WAF-D-15-0123.1.

Kumjian, M. R., 2013a: Principles and applications of dual-polarization weather radar. Part I: Description of the polarimetric radar variables. *J. Oper. Meteor.*, **1**, 226–242, https://doi.org/10.15191/nwajom.2013.0119.

——, 2013b: Principles and applications of dual-polarization weather radar. Part II: Warm and cold season applications. *J. Oper. Meteor.*, **1**, 243–264, https://doi.org/10.15191/nwajom.2013.0120.

——, 2013c: Principles and applications of dual-polarization weather radar. Part III: Artifacts. *J. Oper. Meteor.*, **1**, 265–274, https://doi.org/10.15191/nwajom.2013.0121.

——, and K. A. Lombardo, 2017: Insights into the evolving microphysical and kinematic structure of northeastern U.S. winter storms from dual-polarization Doppler radar. *Mon. Wea. Rev.*, **145**, 1033–1061, https://doi.org/10.1175/MWR-D-15-0451.1.

——, A. V. Ryzhkov, H. D. Reeves, and T. J. Schuur, 2013: A dual-polarization radar signature of hydrometeor refreezing in winter storms. *J. Appl. Meteor. Climatol.*, **52**, 2549–2566, https://doi.org/10.1175/JAMC-D-12-0311.1.

——, S. Mishra, S. E. Giangrande, T. Toto, A. V. Ryzhkov, and A. Bansemer, 2016: Polarimetric radar and aircraft observations of saggy bright bands during MC3E. *J. Geophys. Res. Atmos.*, **121**, 3584–3607, https://doi.org/10.1002/2015JD024446.

Landsea, C. W., and J. L. Franklin, 2013: Atlantic hurricane database uncertainty and presentation of a new database format. *Mon. Wea. Rev.*, **141**, 3576–3592, https://doi.org/10.1175/MWR-D-12-00254.1.

Lord, S. J., H. E. Willoughby, and J. M. Piotrowicz, 1984: Role of a parameterized ice-phase microphysics in an axisymmetric, nonhydrostatic tropical cyclone model. *J. Atmos. Sci.*, **41**, 2836–2848, https://doi.org/10.1175/1520-0469(1984)041<2836:ROAPIP>2.0.CO;2.

Marks, F. D., and R. A. Houze, 1987: Inner core structure of Hurricane Alicia from airborne Doppler radar observations. *J. Atmos. Sci.*, **44**, 1296–1317, https://doi.org/10.1175/1520-0469(1987)044<1296:ICSOHA>2.0.CO;2.

——, ——, and J. F. Gamache, 1992: Dual-aircraft investigation of the inner core of Hurricane Norbert. Part I: Kinematic structure. *J. Atmos. Sci.*, **49**, 919–942, https://doi.org/10.1175/1520-0469(1992)049<0919:DAIOTI>2.0.CO;2.

McFarquhar, G. M., H. Zhang, G. Heymsfield, J. Dudhia, J. B. Halverson, R. Hood, and F. Marks, 2006: Factors affecting the

Brought to you by NOAA Central Library | Unauthenticated | Downloaded 01/14/21 02:34 PM UTC

evolution of Hurricane Erin and the distributions of hydrometeors: Role of microphysical processes. *J. Atmos. Sci.*, **63**, 127–150, https://doi.org/10.1175/JAS3590.1.

——, B. F. Jewett, S. Nesbitt, M. Gilmore, and T.-L. Hsieh, 2012: Vertical velocity and microphysical distributions related to the rapid intensification of Hurricane Dennis (2005). *J. Atmos. Sci.*, **69**, 3515–3534, https://doi.org/10.1175/JAS-D-12-016.1.

Molinari, J., and D. Vollaro, 1989: External influences on hurricane intensity. Part I: Outflow layer eddy angular momentum fluxes. *J. Atmos. Sci.*, **46**, 1093–1105, https://doi.org/10.1175/1520-0469(1989)046<1093:EIOHIP>2.0.CO;2.

Montgomery, M. T., M. E. Nicholls, T. A. Cram, and A. B. Saunders, 2006: A vortical hot tower route to tropical cyclogenesis. *J. Atmos. Sci.*, **63**, 355–386, https://doi.org/10.1175/JAS3604.1.

Murphy, A. M., A. Ryzhkov, and P. Zhang, 2020: Columnar vertical profile (CVP) methodology for validating polarimetric radar retrievals in ice using in situ aircraft measurements. *J. Atmos. Oceanic Technol.*, **37**, 1623–1642, https://doi.org/10.1175/JTECH-D-20-0011.1.

Nguyen, L. T., R. Rogers, J. Zawislak, and J. A. Zhang, 2020: Assessing the influence of convective downdrafts and surface enthalpy fluxes on tropical cyclone intensity change in moderate shear. *Mon. Wea. Rev.*, **147**, 3519–3534, https://doi.org/10.1175/MWR-D-18-0461.1.

NOAA/NWS/ROC, 1991: NOAA Next Generation Radar (NEXRAD) level II base data. NOAA National Centers for Environmental Information, accessed May 2017 to May 2018, https://doi.org/10.7289/V5W9574V.

Reasor, P. D., and M. T. Montgomery, 2001: Three-dimensional alignment and corotation of weak, TC-like vortices via linear vortex Rossby waves. *J. Atmos. Sci.*, **58**, 2306–2330, https://doi.org/10.1175/1520-0469(2001)058<2306:TDAACO>2.0.CO;2.

——, ——, F. D. Marks, and J. F. Gamache, 2000: Low-wavenumber structure and evolution of the hurricane inner core observed by airborne dual-Doppler radar. *Mon. Wea. Rev.*, **128**, 1653–1680, https://doi.org/10.1175/1520-0493(2000)128<1653:LWSAEO>2.0.CO;2.

——, ——, and L. D. Grasso, 2004: A new look at the problem of tropical cyclones in vertical shear flow: Vortex resiliency. *J. Atmos. Sci.*, **61**, 3–22, https://doi.org/10.1175/1520-0469(2004)061<0003:ANLATP>2.0.CO;2.

——, M. D. Eastin, and J. F. Gamache, 2009: Rapidly intensifying Hurricane Guillermo (1997). Part I: Low-wavenumber structure and evolution. *Mon. Wea. Rev.*, **137**, 603–631, https://doi.org/10.1175/2008MWR2487.1.

——, R. Rogers, and S. Lorsolo, 2013: Environmental flow impacts on tropical cyclone structure diagnosed from airborne Doppler radar composites. *Mon. Wea. Rev.*, **141**, 2949–2969, https://doi.org/10.1175/MWR-D-12-00334.1.

Rogers, R., S. Chen, J. Tenerelli, and H. Willoughby, 2003: A numerical study of the impact of vertical shear on the distribution of rainfall in Hurricane Bonnie (1998). *Mon. Wea. Rev.*, **131**, 1577–1599, https://doi.org/10.1175//2546.1.

——, J. A. Zhang, J. Zawislak, H. Jiang, G. R. Alvey III, E. J. Zipser, and S. N. Stevenson, 2016: Observations of the structure and evolution of Hurricane Edouard (2014) during intensity change. Part II: Kinematic structure and the distribution of deep convection. *Mon. Wea. Rev.*, **144**, 3355–3376, https://doi.org/10.1175/MWR-D-16-0017.1.

Rozoff, C. M., C. S. Velden, J. Kaplan, J. P. Kossin, and A. J. Wimmers, 2015: Improvements in the probabilistic prediction of tropical cyclone rapid intensification with passive microwave observations. *Wea. Forecasting*, **30**, 1016–1038, https://doi.org/10.1175/WAF-D-14-00109.1.

Ryzhkov, A. V., and D. S. Zrnić, 1998: Discrimination between rain and snow with a polarimetric radar. *J. Appl. Meteor.*, **37**, 1228–1240, https://doi.org/10.1175/1520-0450(1998)037<1228:DBRASW>2.0.CO;2.

——, and ——, 2019: *Radar Polarimetry for Weather Observations*. 1st ed. Springer, 486 pp., https://doi.org/10.1007/978-3-030-05093-1.

——, ——, and B. A. Gordon, 1998: Polarimetric method for ice water content determination. *J. Appl. Meteor.*, **37**, 125–134, https://doi.org/10.1175/1520-0450(1998)037<0125:PMFIWC>2.0.CO;2.

——, S. E. Giangrande, V. M. Melnikov, and T. J. Schuur, 2005a: Calibration issues of dual-polarization radar measurements. *J. Atmos. Oceanic Technol.*, **22**, 1138–1155, https://doi.org/10.1175/JTECH1772.1.

——, T. J. Schuur, D. W. Burgess, P. L. Heinselman, S. E. Giangrande, and D. S. Zrnić, 2005b: The Joint Polarization Experiment: Polarimetric rainfall measurements and hydrometeor classification. *Bull. Amer. Meteor. Soc.*, **86**, 809–824, https://doi.org/10.1175/BAMS-86-6-809.

——, P. Zhang, H. Reeves, M. Kumjian, T. Tschallener, S. Trömel, and C. Simmer, 2016: Quasi-vertical profiles—A new way to look at polarimetric radar data. *J. Atmos. Oceanic Technol.*, **33**, 551–562, https://doi.org/10.1175/JTECH-D-15-0020.1.

——, P. Bukovcic, A. Murphy, P. Zhang, and G. McFarquhar, 2018: Ice microphysical retrievals using polarimetric radar data. *10th European Conf. on Radar in Meteorology and Hydrology*, the Netherlands, KNMI, 40, projects.knmi.nl/erad2018/ERAD2018_extended_abstract_040.pdf.

——, J. Snyder, J. Carlin, A. Khain, and M. Pinsky, 2020: What polarimetric weather radars offer to cloud modelers: Forward radar operators and microphysical/thermodynamical retrievals. *Atmosphere*, **11**, 362, https://doi.org/10.3390/atmos11040362.

Schecter, D. A., M. T. Montgomery, and P. D. Reasor, 2002: A theory for the vertical alignment of a quasigeostrophic vortex. *J. Atmos. Sci.*, **59**, 150–168, https://doi.org/10.1175/1520-0469(2002)059<0150:ATFTVA>2.0.CO;2.

Schuur, T. J., A. V. Ryzhkov, and D. R. Clabo, 2005: Climatological analysis of DSDS in Oklahoma as revealed by 2D-video disdrometer and polarimetric WSR-88D. *32nd Conf. on Radar Meteorology*, Albuquerque, NM, Amer. Meteor. Soc., 15R.4, https://ams.confex.com/ams/pdfpapers/95995.pdf.

Seliga, T. A., and V. N. Bringi, 1978: Differential reflectivity and differential phase shift: Applications in radar meteorology. *Radio Sci.*, **13**, 271–275, https://doi.org/10.1029/RS013i002p00271.

Sitkowski, M., J. P. Kossin, and C. M. Rozoff, 2011: Intensity and structure changes during hurricane eyewall replacement cycles. *Mon. Wea. Rev.*, **139**, 3829–3847, https://doi.org/10.1175/MWR-D-11-00034.1.

Starzec, M., C. R. Homeyer, and G. L. Mullendore, 2017: Storm Labeling in Three Dimensions (SL3D): A volumetric radar echo and dual-polarization updraft classification algorithm. *Mon. Wea. Rev.*, **145**, 1127–1145, https://doi.org/10.1175/MWR-D-16-0089.1.

Stern, D., and D. Nolan, 2009: Reexamining the vertical structure of tangential winds in tropical cyclones: Observations and theory. *J. Atmos. Sci.*, **66**, 3579–3600, https://doi.org/10.1175/2009JAS2916.1.

——, and ——, 2012: On the height of the warm core in tropical cyclones. *J. Atmos. Sci.*, **69**, 1657–1680, https://doi.org/10.1175/JAS-D-11-010.1.

Stevenson, S. N., K. L. Corbosiero, and J. Molinari, 2014: The convective evolution and rapid intensification of Hurricane

Brought to you by NOAA Central Library | Unauthenticated | Downloaded 01/14/21 02:34 PM UTC

Earl (2010). *Mon. Wea. Rev.*, **142**, 4364–4380, https://doi.org/10.1175/MWR-D-14-00078.1.

Straka, J. M., D. S. Zrnić, and A. V. Ryzhkov, 2000: Bulk hydrometeor classification and quantification using polarimetric radar data: Synthesis of relations. *J. Appl. Meteor.*, **39**, 1341–1372, https://doi.org/10.1175/1520-0450(2000)039<1341:BHCAQU>2.0.CO;2.

Tobin, D. M., and M. R. Kumjian, 2017: Polarimetric radar and surface-based precipitation-type observations of ice pellet to freezing rain transitions. *Wea. Forecasting*, **32**, 2065–2082, https://doi.org/10.1175/WAF-D-17-0054.1.

Trömel, S., M. R. Kumjian, A. V. Ryzhkov, C. Simmer, and M. Diederich, 2013: Backscatter differential phase—Estimation and variability. *J. Appl. Meteor. Climatol.*, **52**, 2529–2548, https://doi.org/10.1175/JAMC-D-13-0124.1.

——, A. V. Ryzhkov, P. Zhang, and C. Simmer, 2014: Investigations of backscatter differential phase in the melting layer. *J. Appl. Meteor. Climatol.*, **53**, 2344–2359, https://doi.org/10.1175/JAMC-D-14-0050.1.

Uhlhorn, E. W., B. W. Klotz, T. Vukicevic, P. D. Reasor, and R. F. Rogers, 2014: Observed hurricane wind speed asymmetries and relationships to motion and environmental shear. *Mon. Wea. Rev.*, **142**, 1290–1311, https://doi.org/10.1175/MWR-D-13-00249.1.

Van Den Broeke, M. S., 2013: Polarimetric radar observations of biological scatterers in Hurricanes Irene (2011) and Sandy (2012). *J. Atmos. Oceanic Technol.*, **30**, 2754–2767, https://doi.org/10.1175/JTECH-D-13-00056.1.

——, D. M. Tobin, and M. R. Kumjian, 2016: Polarimetric radar observations of precipitation type and rate from the 2–3 March 2014 winter storm in Oklahoma and Arkansas. *Wea. Forecasting*, **31**, 1179–1196, https://doi.org/10.1175/WAF-D-16-0011.1.

Wang, J., and Coauthors, 2015: A long-term, high-quality, high-vertical resolution GPS dropsonde dataset for hurricane and other studies. *Bull. Amer. Meteor. Soc.*, **96**, 961–973, https://doi.org/10.1175/BAMS-D-13-00203.1.

Wang, M., K. Zhao, M. Xue, G. Zhang, S. Liu, L. Wen, and G. Chen, 2016: Precipitation microphysics characteristics of a Typhoon Matmo (2014) rainband after landfall over eastern China based on polarimetric radar observations. *J. Geophys. Res. Atmos.*, **121**, 12 415–12 433, https://doi.org/10.1002/2016JD025307.

——, ——, W.-C. Lee, and F. Zhang, 2018: Microphysical and kinematic structure of convective-scale elements in the inner rainband of Typhoon Matmo (2014) after landfall. *J. Geophys. Res. Atmos.*, **123**, 6549–6564, https://doi.org/10.1029/2018JD028578.

——, ——, Y. Pan, and M. Xue, 2020: Evaluation of simulated drop size distributions and microphysical processes using polarimetric radar observations for landfalling Typhoon Matmo (2014). *J. Geophys. Res. Atmos.*, **125**, e2019JD031527, https://doi.org/10.1029/2019JD031527.

Wen, L., and Coauthors, 2018: Drop size distribution characteristics of seven typhoons in China. *J. Geophys. Res. Atmos.*, **123**, 6529–6548, https://doi.org/10.1029/2017JD027950.

Willis, P. T., and A. J. Heymsfield, 1989: Structure of the melting layer in mesoscale convective system stratiform precipitation. *J. Atmos. Sci.*, **46**, 2008–2025, https://doi.org/10.1175/1520-0469(1989)046<2008:SOTMLI>2.0.CO;2.

Willoughby, H. E., F. D. Marks, and R. J. Feinberg, 1984: Stationary and moving convective bands in hurricanes. *J. Atmos. Sci.*, **41**, 3189–3211, https://doi.org/10.1175/1520-0469(1984)041<3189:SAMCBI>2.0.CO;2.

Wolff, D. B., W. A. Petersen, A. Tokay, D. A. Marks, and J. L. Pippitt, 2019: Assessing dual-polarization radar estimates of extreme rainfall during Hurricane Harvey. *J. Atmos. Oceanic Technol.*, **36**, 2501–2520, https://doi.org/10.1175/JTECH-D-19-0081.1.

Wu, D., and Coauthors, 2018: Kinematics and microphysics of convection in the outer rainband of Typhoon Nida (2016) revealed by polarimetric radar. *Mon. Wea. Rev.*, **146**, 2147–2159, https://doi.org/10.1175/MWR-D-17-0320.1.

Zipser, E. J., and K. R. Lutz, 1994: The vertical profile of radar reflectivity of convective cells: A strong indicator of storm intensity and lightning probability? *Mon. Wea. Rev.*, **122**, 1751–1759, https://doi.org/10.1175/1520-0493(1994)122<1751:TVPORR>2.0.CO;2.

Zrnić, D. S., and A. V. Ryzhkov, 1999: Polarimetry for weather surveillance radars. *Bull. Amer. Meteor. Soc.*, **80**, 389–406, https://doi.org/10.1175/1520-0477(1999)080<0389:PFWSR>2.0.CO;2.

——, N. Balakrishnan, C. L. Ziegler, V. N. Bringi, K. Aydin, and T. Matejka, 1993: Polarimetric signatures in the stratiform region of a mesoscale convective system. *J. Appl. Meteor.*, **32**, 678–693, https://doi.org/10.1175/1520-0450(1993)032<0678:PSITSR>2.0.CO;2.

Brought to you by NOAA Central Library | Unauthenticated | Downloaded 01/14/21 02:34 PM UTC